Spring 5-17-2017

Particle Enrichment in Longitudinal Standing Bulk Acoustic Wave Microfluidics

Mingyang Cui
Washington University in St Louis

WASHINGTON UNIVERSITY IN ST. LOUIS

School of Engineering and Applied Science
Department of Mechanical Engineering and Materials Science

Thesis Examination Committee:
J. Mark Meacham, Chair
Amit Pathak
David Peters

Particle Enrichment in Longitudinal Standing Bulk Acoustic Wave Microfluidics

by
Mingyang Cui

A thesis presented to
School of Engineering and Applied Science
of Washington University in
partial fulfillment of the
requirements for the degree
of Master of Science

May 2017
St. Louis, Missouri

Table of Contents

List of Figures

List of Tables

Acknowledgments

I would like to express my appreciation to those who helped me with various aspects of this thesis research, particularly those in the Scalable Integrated MicroSystems lab at Washington University in St. Louis. First, I want to thank Professor J. Mark Meacham for his guidance and patience throughout my research. His numerous perspectives on microfluidics, from the theoretical to the applied, inspired and encouraged me to explore the topic in more depth.

I would also like to thank Michael Binkley for his contributions to my work, from the very beginning to the very end. Michael's exceptional creativity, combined with his experience in design and conduct of experiments helped me finish one of the most important parts of this thesis, experimental validation of my modeling work. I would like to thank Minji Kim and Andrew Ledbetter for thoughtful exchange of ideas during this project. Their knowledge of physics and computational modeling proved beneficial to my own modeling efforts.

Finally, I would like to thank my parents and sister, Yonghua Cui, Ping Zhao and Xin Zhao, without whom none of this work would have been possible, providing me the freedom to follow my own path in life and supporting the choices that I have made.

Mingyang Cui

Washington University in St. Louis

May 2017

Dedicated to my grandparents: Wenhua Zhao and Xiangting Wei

ABSTRACT

Particle Enrichment in Longitudinal Standing Bulk Acoustic Wave Microfluidics

by

Mingyang Cui

Master of Science in Mechanical Engineering

Washington University in St. Louis, 2017

Research Advisor: Professor J. Mark Meacham

Separation, isolation, and enrichment of targeted nano- and microparticles are critical to a variety of biomedical applications from clinical research (development of therapeutics and diagnostics) to fundamental investigations that require concentration of specific cells from culture, separation of target species from heterogenous mixtures, or controlled perturbation of cells and microorganisms to determine their response to stimuli. Numerous techniques are available for bench-scale and medical settings; however, these traditional approaches are often labor intensive, time-consuming, costly, and/or require modification of the target. Efficiency and specificity are also lacking. Recently, techniques that exploit the similar scales of microfluidic technologies and the intrinsic properties of cells have allowed for increased automation, reduced reagent waste, and decreased cost, as well as improved performance. So-called lab-on-a-chip (LOC) approaches enable rapid fabrication and optimization of small-scale, low-volume microchannels capable of high performance enrichment and separation owing to precise control of the forces driving the manipulation. Depending on the physics underlying a particular method, devices are classified as optical, hydrodynamic, dielectrophoretic, magnetic, or acoustic.

Acoustics, and specifically ultrasound, permits noncontact cell separation and retention, which reduces the potential for undesirable surface interactions and physical stress on sensitive biological samples. Typically, separation is achieved by pinning a standing wave perpendicular (conventional lateral acoustophoresis) or parallel (longitudinal acoustic trapping) to the direction of flow. In this thesis, we report a novel longitudinal standing bulk acoustic wave (LSBAW) microfluidic channel that incorporates pairs of pillar arrays oriented perpendicular to the inflow direction. The pillar arrays act as 'pseudo walls' that locally amplify the pressure in the enrichment zone, which can be tuned to overcome the drag force for particles of size greater than a critical diameter. Thus, these particles are preferentially retained within the nodes of the local pressure field. In our study, model predictions were used to guide experimental trapping of particles in microchannels with two pillar configurations.

We created six different microfluidic channels with varying inlet/outlet geometries, widths, and pillar shapes. Model results showed pressure field amplification caused by the 'pseudo walls' bounding the enrichment zone of each design. We also demonstrated trapping of polystyrene beads (5 μm and 20 μm) and 10 μm fluorescent hollow glass spheres during actuation at various predicted half-wave resonances of these devices. Certain channel architectures achieved acoustic field amplification suitable for particle trapping at flow rates up to ~20 μL/min. In addition, the simulated pressure fields (eigenmodes) were consistent with experimentally observed mode shapes, which validated our modeling approach. Computational and experimental results suggest that LSBAW pillar geometries and flow parameters can be tuned to achieve enhanced enrichment of targeted particles in a predefined region.

Chapter 1: Introduction

1.1 Manipulation of Particles in Biomedical Research

Manipulation of nano- and microparticles suspended in fluids is essential in many biomedical applications from fundamental molecular and cellular biology to clinical medicine. Effective separation, isolation, enrichment, and purification of cells from complex biofluids is particularly important in emerging approaches to improve disease diagnosis and therapy (e.g., the liquid biopsy). In addition, enrichment is critical to obtain a measurable quantity of the species of interest, which is often at a low concentration relative to a complex background sample. For example, blood is a blend of various cells that requires the enrichment and separation of a few desired cells (red blood cells (RBCs), white blood cells (WBCs) or potentially circulating tumor cells (CTCs)) to accurately determine its character and condition [1].

Numerous techniques to separate and enrich bioparticles and cells have been developed for bench-scale and clinical settings. These inherently high-volume (macroscale) techniques achieve separation based either on the physical properties of cells, such as size, density or compressibility, or on cell affinity, which relies on electrical, chemical, magnetic or adhesive properties specific to each cell type [1]. Among these, the most prevalent commercially available methods are based on adherence, density and antibody binding. Adhesion-based techniques are useful if the main requirement is only the isolation of adherent cells. Centrifugation techniques are useful to pre-enrich specific cells within samples that feature populations of cells with different sizes and/or densities prior to further separation and/or analysis. Due to their high specificity, antibody-mediated separation methods are currently the gold standard for isolation of unique cell populations. Unfortunately, available macroscale techniques are often labor-

intensive, time-consuming or costly, or require additional labels and tags to identify cells. Further, without modification of a target of interest, these methods do not provide adequate efficiency or specificity. Emerging techniques that exploit the dimensional similarity between the length scale of cells (~1 to 10s of μm) and that of miniaturized devices (~10s to 100s of μm) have recently been applied to the biomedical field. These microfluidic and integrated lab-on-a-chip (LOC) technologies better utilize the inherent properties of the cells to allow for contact-free, automated, and lower-cost alternatives to macroscale processes.

1.2 Lab-on-a-chip Technologies

Miniaturization enables high performance enrichment and separation due to precise and accurate control of the forces driving the nano-/microparticle manipulation. Depending on the physics underlying a particular method, devices are classified as optical, hydrodynamic, dielectrophoretic, magnetic, or acoustic. It is important to compare these methods to identify the best-suited technology to meet the requirements of a given application. For example, methods that avoid use of biochemical labels are preferred as labeling increases processing time and expense, and not all cell types are amenable to labeling. Whole blood diagnostics typically require the separation of blood components (plasma, RBCs, WBCs, and platelets) prior to analysis; however, separations involving blood cell labeling prove challenging as there is a lack of consensus on the biochemical markers of relevant cells (e.g., WBCs and CTCs) [2]. Here, reduction in variability of a heterogeneous sample (e.g., by fractionating cells into homogenous subpopulations) facilitates isolation and analysis. Fractionation is critical for polydisperse cell types such as WBCs and cancer cells where cell composition is relatively constant, but differences in size can be exploited for separation without known biomarkers. Noncontact operation is also desirable to reduce the risk of clogging in enrichment zones, to minimize loss of

particles that might otherwise stick to surfaces, and to decrease the possibility of contamination in sample preparation.

To make fair comparisons of different microfluidic systems, multiple aspects must be considered including system complexity, buffer demands, and discriminating parameters (size, density, compressibility, electrical polarizability). Various classes of microfluidic separation are summarized in Table 1.1. Due to its relevance to the present study, acoustofluidic enrichment is discussed in greater detail below.

Table 1.1 General comparison of microfluidic trapping methods

Technology	Mode of Separation	Separation Criteria	System Complexity (noncontact)	System Complexity (contact)	Reference
Hydrodynamic	Streamline manipulation	Size, shape	Low	Low	[3,4]
Dielectrophoretic	Dielectrophoretic force	Polarizability, size	Medium	Low	[5-8]
Magnetic	Differential magnetophoretic mobility	Intrinsic magnetic susceptibility	High	Low	[9-13]
Optical	Optical lattice	Refractive index, size	High/Medium	Scarcely operated in contact mode	[14-18]
Acoustic	Acoustic radiation force	Size, density, compressibility	Low	Scarcely operated in contact mode	[19-25]

1.3 Acoustofluidic Enrichment

Acoustic microfluidics allow noncontact separation and enrichment of nano-/microparticles, which reduces unwanted surface interactions and physical stress on sensitive samples in biomedical applications. Particles suspended in a liquid migrate to the pressure minima (nodes) or maxima (antinodes) when placed in a standing acoustic field. Acoustic radiation forces arise

due to the acoustic impedance mismatch between particles and suspension medium. The magnitude and direction of these forces depend on the strength of the acoustic pressure field, as well as particle geometric parameters (shape and volume) and material acoustic contrast factors (material-dependent) [26]. Coakley et al. [27] and Hertz [28] reported a pioneering device for macroscale cell and particle manipulation. Recently, macroscopic approaches to acoustofluidic separation and enrichment have been miniaturized to achieve greater efficiency and specificity. For example, Petersson et al. [29, 30] developed an acoustic microfluidic channel that can separate RBCs from lipid microemboli with a separation efficiency greater than 95%.

In conventional free-flow acoustophoresis, a standing wave is generated between two sidewalls of a microfluidic channel, and lateral separation occurs as particles transit in the direction of fluid flow. Particles with positive acoustic contrast factor (e.g., cells and most microparticles) move to the nodes, while particles with negative acoustic contrast factor (e.g., lipids, gas-filled microspheres) move to the antinodes; thus, one or both lateral dimensions of the microfluidic channel are constrained to 1 mm or smaller by the flow separation orthogonality [30,31]. Longitudinal acoustic trapping uses a standing ultrasonic wave in parallel with the flow channel yielding multiple nodal locations along the direction of flow. In the vicinity of these pressure minima, acoustic radiation forces F_{ac} opposes viscous drag F_d to preferentially trap and enrich particles that exceed a threshold size [20-22].

1.4 Thesis Overview

In this work, we present a novel longitudinal acoustic trap that extends this concept to incorporate pairs of pillar arrays oriented perpendicular to the flow direction. These perforated ‘pseudo walls’ form a longitudinal standing bulk acoustic wave (LSBAW) enrichment structure that locally augments the pressure field to retain particles at a single predefined location along

the channel (Figure 1.1). In this thesis, I demonstrate the LSBAW concept by presenting computational and experimental results for several different microchannel geometries and pillar configurations totaling six devices. Initial results suggest that LSBAW pillar geometries and flow parameters can be tuned to achieve targeted enrichment in a scalable microfluidic channel.

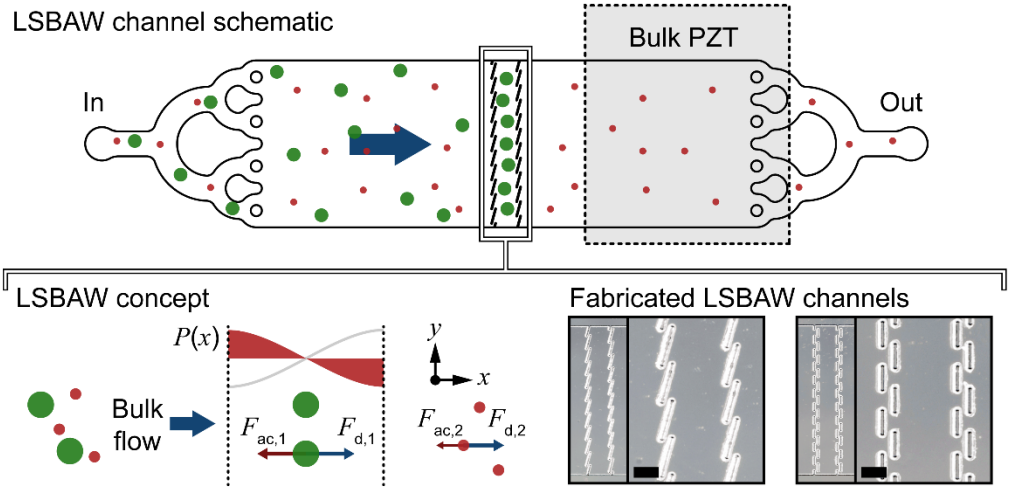

Figure 1.1 Longitudinal standing bulk acoustic wave (LSBAW) enrichment platform: schematic overview, enrichment concept, and representative fabricated channels for experimental evaluation

Chapter 2: Theory, Modeling and Experimental Methods

2.1 Acoustofluidics Theory

Acoustofluidics describes the incorporation and exploitation of acoustic phenomena in microfluidic systems. The characteristic wavelength of ultrasound in water is of a similar order to the length scales of most microfluidic devices (from 1 to 10s to 100s of μm) enabling manipulation of fluids and suspended microparticles in ways that are not possible with other lab-on-a-chip (LOC) technologies. The primary advantages of acoustofluidic actuation are its precise microscale control and gentle noncontact nature [32]. In this chapter, various aspects of acoustofluidics are described with emphasis on those most relevant to acoustic separation and enrichment.

2.1.1 Microfluidics

Microfluidics is a class of fluidic system wherein a fluid is confined in at least one dimension to the microscale domain. Today, microfluidic technologies often comprise essential components of LOC or micro total analysis systems (μTAS). These technologies are attractive for several reasons: low power consumption, inherently laminar flow, short reaction and analysis times, small sample volumes and potential for low manufacturing cost.

Scaling laws

Tabeling [33] and Bruus [34] provide detailed discussions of scaling in microfluidic domains. Scaling laws express how physical quantities vary with the size of a given system or subject, while keeping quantities such as time, pressure, temperature, etc. constant. As an example, consider body forces, such as gravity and inertia, and surface forces, such as surface tension and viscosity. The basic scaling law for the ratio of these two types of forces can be expressed as

$$\frac{\text{volume forces}}{\text{surface forces}} \propto \frac{l^3}{l^2} = l \overset{l \to 0}{\longrightarrow} 0 \tag{1}$$

This scaling law implies that as we decrease the length scale *l* of a system to the microscale, the ratio of volume forces to surface forces goes to zero. Thus, volume forces, which are important at the macroscale, become largely unimportant at the microscale. Instead, surface forces become dominant. The most essential implication of this law is that viscous effects dominate over inertia in microfluidics, which render the fluid flow laminar.

Laminar flow

Laminar flow, as opposed to turbulent or chaotic flow, is characterized by fluid flowing without lateral mixing between adjacent laminae and by high momentum diffusion with low momentum advection [35]. The Reynolds number Re, which predicts whether a flow will be laminar or turbulent, is defined as:

$$Re = \frac{\rho v d}{\eta} \tag{2}$$

where ρ is fluid density, v is characteristic flow velocity, d is characteristic length, and η is fluid viscosity. For a typical microfluidic system, the Reynolds number is less than or approximately unity, which often allows for analytical determination of the flow profile and other hydrodynamic parameters of interest.

Stokes drag

As a particle moves relative to a liquid medium, its motion is opposed by viscous drag. Under laminar flow conditions, in which non-linear terms are expected to be negligible and where there is a no-slip boundary condition on the particle surface, viscous drag F_{drag} on the particle can be calculated using Stokes drag:

$$F_d = 6\pi\eta a v \tag{3}$$

where η is fluid viscosity, a is particle radius, and v is characteristic flow velocity [35]. Therefore, for purposes of this thesis, drag is proportional to radius. The drag force carries particles along in a fluid flow, and will also counteract motion induced by an acoustic field or other external forces.

Gravity

In microfluidic systems, volume (or body) forces, such as gravity, are often neglected; however, when the particles in a medium are denser than the medium, particles can settle to the bottom of a channel given sufficient residence time. Polystyrene beads and glass microspheres under consideration here sink slowly as the particle density is only slightly greater than that of water. Assuming terminal velocity for sedimentation is reached instantaneously, particle settling time is given by:

$$t = \frac{9\eta h}{2(\rho_p - \rho)a^2 g} \tag{4}$$

where, η is fluid viscosity, h is the channel height, ρ_p is the particle density, ρ is the fluid density, and g is the gravitational constant [34]. After determining a characteristic settling time, researchers can incorporate a vertical ultrasonic force (or levitation) to offset particle sedimentation. For our purposes (i.e., for the time scales relevant to current investigations), gravity and particle settling are neglected.

2.1.2 Ultrasonic Acoustics

Sound is the propagation of a deviation from static conditions in a mechanical property of a medium [36]. The property can be velocity or displacement of particles in a medium as a function of time and space, or stress and strain, which in fluids yields the sound pressure field,

one of the most essential parameters in acoustofluidics. The pressure field is typically found by solving the wave equation. Due to the characteristic lengths involved, ultrasound is employed in acoustic microfluidics. Operating frequencies exceed 0.5 MHz, which is well above the audible threshold, and most devices operate between 0.5 and 20 MHz. Sound (vibration) behaves differently in fluids than in solids, and as sound propagation in fluids is most relevant to the current work it will be emphasized in the following sections.

Ultrasound in fluids

The description of sound in a fluid is mathematically simpler than that of sound in solids, the main reason being that a fluid deforms continuously under shear stress. Normal stress can exist in a great degree, which leads to an expression for pressure. The pressure induced by sound is different from the more familiar hydrostatic fluid pressure. In a microfluidic system, where a fluid is usually treated as incompressible, hydrostatic pressure is assumed constant throughout the system. Thus, the pressure as discussed in this thesis, if not specified, refers to sound pressure. In addition, we also assume that the bulk velocity of fluid is much smaller than the speed of sound. The basic acoustic theory presented here is based largely on acoustics texts by Blackstock [36] and Kingsler [37].

We first introduce velocity potential, which relates to the pressure and velocity field as:

$$t\boldsymbol{v}(\boldsymbol{r},t) = \nabla\varphi(\boldsymbol{r},t) \tag{5}$$

$$p(\boldsymbol{r},t) = -\rho\frac{\partial}{\partial t}\varphi(\boldsymbol{r},t) \tag{6}$$

where $\boldsymbol{v}$ is the velocity of displacement at position $\boldsymbol{r}$ and time t. p is the sound pressure, and ρ is the density of the fluid medium. The velocity potential satisfies the wave equation for describing the sound field, so we have:

$$\nabla^2\varphi = \frac{1}{c^2}\frac{\partial^2\varphi}{\partial t^2} \tag{7}$$

where c is the speed of sound in the fluid. The speed of sound in the fluid is one of the key parameters in problems of interest and is found from the compressibility κ and density of the fluid ρ:

$$c = \frac{1}{\sqrt{\kappa\rho}} = \sqrt{\frac{K}{\rho}} \tag{8}$$

where K is the bulk modulus, which is more widely used in solid mechanics and materials science than compressibility.

In this work, we neglect effects of viscosity of the fluid. In reality, fluid viscosity gives rise to damping of the sound field due to viscous losses in the fluid; however, for aqueous mixtures and ultrasound at MHz frequencies, this effect should be minimal.

Radiation Force

When a particle is immersed in a fluid medium and subjected to a sound field, it will be acted upon by time-averaged (steady-state) forces due to the differences in acoustic properties of a particle and the fluid medium (i.e., acoustic impedance mismatch). Two kinds of radiation force are significant in acoustic microfluidic particle manipulation: the primary radiation force and the secondary radiation force. To simplify this analysis, it is assumed that spherical polymer microbeads or cells with positive acoustic contrast are immersed in water and subjected to an ultrasonic standing wave. The primary radiation force tends to drive the particles towards the zero pressure nodes of the field, and the secondary acoustic radiation force is an attractive interparticle force that tends to agglomerate the particles. We will discuss these two radiation forces separately, based on seminal work reported in the early to mid 20th century [38-40].

Primary Radiation Force

The most commonly used expression for the forces acting on particles in an arbitrary sound field is given by Gor'kov [40]. For a spherical particle with radius a in an inviscid fluid (i.e., neglecting viscous effects and heat conduction in the fluid), the primary radiation force is expressed by the gradient of both pressure and velocity fields:

$$F_{rad} = -\frac{4\pi a^3}{3}\left[f_1 \frac{\kappa}{2}\nabla\langle p^2\rangle - \ f_2 \frac{3\rho}{4}\nabla\langle v^2\rangle\right] \tag{9}$$

Parameters f_1 and f_2 are functions of relevant material parameters of the medium and fluid, defined as:

$$f_1 = 1 - \frac{\kappa_p}{\kappa} \tag{10}$$

$$f_2 = \frac{2(\rho_p - \rho)}{2\rho_p + \rho} \tag{11}$$

where κ is compressibility, index "p" refers to parameters pertaining to the particle (otherwise pertaining to the fluid). It is important to note that f_1 is determined by the compressibility difference and couples to the pressure gradient, and f_2 is determined by the density difference and couples to the velocity gradient.

As stated earlier, it is the primary acoustic radiation force that drives particles to the nodes or antinodes of the pressure field, but it is the acoustic contrast factor that determines whether particles move to the nodes (minimum pressure) or antinodes (maximum pressure). The acoustic contrast factor Φ is calculated as follows:

$$\Phi = \frac{f_1}{3} + \frac{f_2}{2} \tag{12}$$

Particles with a positive acoustic contrast are driven to nodes when subjected to an ultrasonic standing wave, while particles with a negative acoustic contrast factor are driven to antinodes. Polystyrene beads have a density of 1060 kg/m^3 and a compressibility of 2.16×10^{-10} Pa^{-1}, whereas water, which is representative of the fluids used in the reported work, has a density of 998 kg/m^3 and a compressibility of 4.56×10^{-10} Pa^{-1}; therefore, the acoustic contrast factor is always positive, which means that the enrichment of these particles will occur at nodes of the pressure fields.

Secondary Radiation Force

If a large number of particles are present in the fluid, which is often the case particularly as particles focus to a single location, each particle will produce a scattered sound field that can influence other adjacent particles. Interactions between these particles give rise to secondary radiation forces. If the incident field is a plane wave in one dimension, the secondary radiation force between two identical spherical particles can be derived as:

$$F_{sec} = 4\pi a^6 \left[\frac{\left(\rho_p - \rho\right)^2 (3\cos^2\theta - 1)}{6\rho d^4} v^2(x) - \frac{\omega^2 \rho \left(\kappa_p - \kappa\right)^2}{9d^2} p^2(x) \right] \qquad (13)$$

where θ is the angle between the line connecting the particle centers and the propagation direction of the incident wave, d is the center-to-center distance between the two particles, and ω is the angular frequency [41]. By convention, a positive secondary radiation force means a repulsive force, while a negative secondary radiation force means an attractive force.

The secondary radiation force is strongly dependent on the distance between the particles. The longer the distance between two particles, the smaller the secondary radiation force, which is often neglected for this reason. In this work, we observe clusters of particles in our enrichment zone suggesting that these effects become significant during particle trapping.

Equation (13) assumes that the incident field is a one-dimensional plane wave, which can be a limitation when applied to complex fields such as those present in LSBAW microfluidic devices; however, since the force is only significant at very short distances, the plane wave approximation is still likely appropriate for these cases. As the drag and primary radiation force are active at the same time, one must consider these two forces and the secondary radiation force together to determine the final positions of the particles, which is an important subject when doing particle tracking in acoustofluidics.

Acoustic Streaming

Acoustic streaming arises due to viscous losses in a fluid and may take one of three forms: Schlichting, Rayleigh, or Eckart streaming [42]. Schlichting streaming is induced by the viscous boundary layer close to a surface and has vortices much smaller than the acoustic wavelength [43]. Rayleigh streaming stems from boundary layers driving streaming vortices on the scale of a quarter wavelength outside of the boundary layer itself [44]. Eckart streaming typically gives flow in the sound propagation direction [45]. In acoustic microfluidic separations, streaming is usually considered undesirable, as it induces drag on the particles, which tends to adversely affect the static trapping in a microfluidic chip. Thoughtful microchannel design is used to minimize acoustic streaming effects. Under certain operating conditions, we observed weak acoustic streaming phenomena in this thesis work; however, under design conditions, streaming does not significantly affect the enrichment field. Therefore, acoustic streaming is neglected in our model analysis.

2.2 Computational Modeling

Computational modeling is used to (1) determine under which conditions strong pressure fields can be established in LSBAW microchannels and (2) to investigate the spatial distribution of

those pressure fields, which exhibit the nodes and antinodes where separation and enrichment occur. Models can predict eigenfrequencies and eigenmodes of interest or the complex harmonic response of a system, thus yielding guidelines for the design and optimization of a particular microfluidic channel. Unlike most acoustofluidic channels used for particle separation, the LSBAW has a complex architecture, which makes this process more challenging. Modeling efforts involve tradeoffs between accuracy and practicality, and geometric complexity increases computational expense necessitating various assumptions and simplifications. It is important that these simplifications are validated such that modeling results provide realistic predictions of device operation. Finite element analysis using COMSOL Multiphysics (v5.2a) has been adopted in this thesis.

2.2.1 Assumptions and Simplifications

A three-dimensional (3D) model best represents the complex geometry of the LSBAW devices; however, 3D modeling proved challenging due to computational expense and limitations of our computing resources. The microchannel includes domains of vastly different scales (pillars with characteristic lengths of ~100s of μm and a 50 μm deep fluid channel in a 63.5 mm x 31.7 mm x 3.0 mm thick glass microchip actuated by a 24 mm x 28 mm x 1.5 mm thick PZT-8 piezoelectric transducer) (Figure 2.1). A dense mesh was required to accurately capture the acoustic field within the enrichment area of the glass channel, and after carefully constructing the mesh in COMSOL, the simulation could not run due to limited computational power.

The 3D model was simplified to a two-dimensional (2D) representation of the LSBAW assembly (Figure 2.2). First, we modeled the system in the horizontal plane, with piezoelectric actuation from a lateral side of the glass chip. The rationale for doing this is that the height of the glass and channel depth are much less than the lateral dimensions. Given that average speed of sound in

water is 1500 m/s, the acoustic wavelength at the highest used frequency $f = 3.3$ MHz is 0.45 mm and is thus 9 times the depth of the channel. Consequently, at relevant frequencies of operation it is impossible to support a standing wave in the vertical direction within the water-filled channel. Unfortunately, the 2D representation of the entire microchannel is not able to realistically capture the behavior of the pillars in the enrichment zone, which are treated as separate from the rest of the solid structure. Therefore, in the 2D model, piezoelectric actuation does not lead to pillar vibration as in the real system.

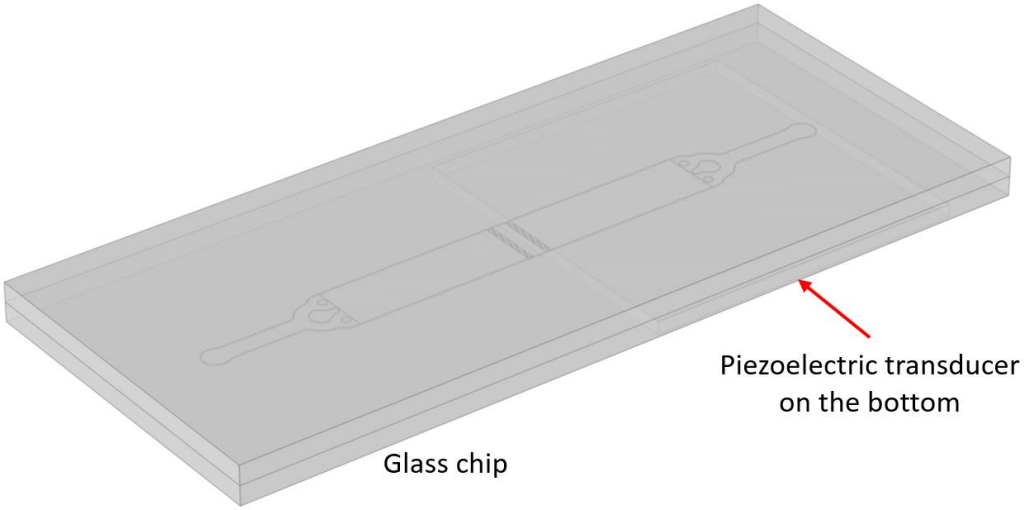

Figure 2.1 3D modeling of LSBAW devices

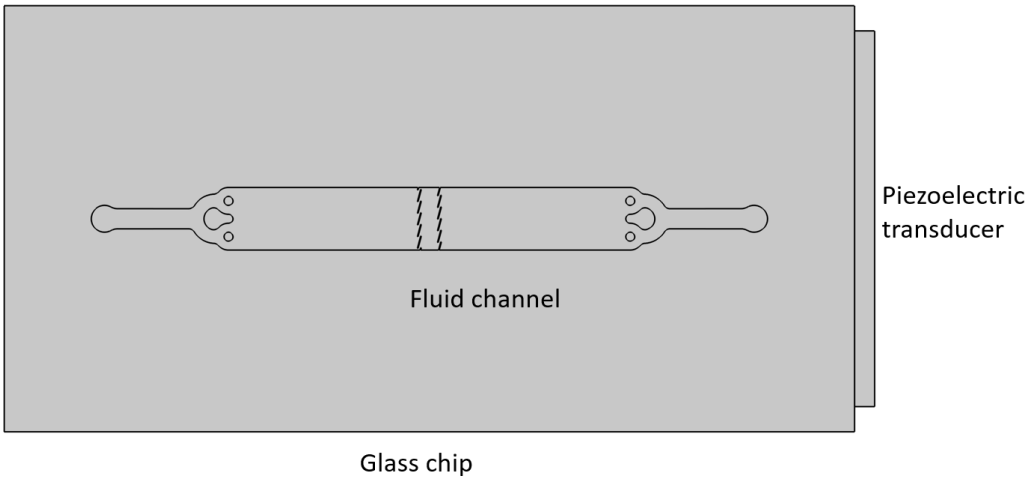

Figure 2.2 2D modeling of LSBAW devices

Eigenfrequency Analysis

To account for the influence of the pillar structures without introducing the computational expense of a 3D approach, the model was further simplified to include only the fluid microchannel domain. Water-glass interfaces at the channel and pillar walls were modeled using a hard-wall condition due to large differences in characteristic acoustic impedance. Viscous and acoustic streaming effects were also neglected [46]. Acoustic waves within the microchannel of an acoustofluidic device are driven by vibrations of the microchannel walls. Therefore, models that are restricted to the fluid domain typically incorporate harmonic displacement boundary conditions at the microchannel walls; however, for a symmetric channel, actuation of this type is not able to capture odd modes due to destructive interference at the channel midline [47]. While our geometry is not strictly symmetric, the pillar arrays appear as nearly parallel walls resulting in a quasi-symmetric configuration; however, we are able to actuate odd harmonics experimentally, which suggests that actuation by wall displacement is not appropriate for modeling LSBAW devices. For this reason, we selected the eigenfrequency study in COMSOL. If all sources are removed from a frequency-domain equation, its solution becomes zero for all

but a discrete set of angular frequencies ω, where the solution has a well-defined shape, but undefined magnitude. These solutions are known as eigenmodes, and the corresponding frequencies are eigenfrequencies [48]. The direct physical significance of the eigenmodes and eigenfrequencies is that they can identify the resonant frequencies of a structure, which is here represented by the fluid chamber. For a given frequency, the resultant mode shape is equivalent to that of the pressure field within the microchannel, though the predicted pressure amplitude is not expected to match experimental values. While it may appear that the problem is oversimplified, the eigenfrequency/eigenmode approach has been shown to accurately predict the qualitative behavior of many acoustic microfluidic devices [49]. Using these assumptions and simplifications, a 2D model describes the principal working mechanism of particle separation and enrichment in LSBAW architectures. In chapter 3, we validate this model by demonstrating consistency between predicted and observed pressure fields of the model and experiments.

2.2.2 Modeling

Application Modules

The eigenfrequency/eigenmode analysis of the fluid chamber was implemented in COMSOL Multiphysics. As stated above, modeling was performed on a 2D domain in the horizontal plane using the *pressure acoustics, frequency domain, eigenfrequency study* to identify potential operating frequencies for a given LSBAW geometry and to determine the pressure field at those frequencies.

Governing Equations

In an eigenfrequency formulation, source terms are absent, so the eigenmodes and eigenfrequencies are found by:

$$\nabla \cdot \left(-\frac{1}{\rho_c}\nabla p\right) + \frac{\lambda^2 p}{\rho_c {c_c}^2} = 0 \tag{14}$$

Materials

The fluid was modeled as water with a density of 998 kg/m^3 and a speed of sound of 1481 m/s. Damping was neglected so the fluid was modeled as inviscid. Incorporation of a complex speed of sound, which can account for viscous damping, may provide a more realistic description of device behavior; however, it was neglected here due to uncertainty in how to best incorporate attenuation effects.

Boundary Conditions

The fluid-structure interaction was modeled as a hard wall condition:

$$-\boldsymbol{n} \cdot \left(-\frac{1}{\rho_c}(\nabla p_t - \boldsymbol{q}_d)\right) = 0 \tag{15}$$

This is widely used in modeling due to the small acoustic impedance ratio $\rho_w c_w / \rho_g c_g = 0.12$ (high mismatch) between water and glass.

Meshing and Solver

We used automatic triangular meshing with element control. The maximum element growth rate was 1.3, the curvature factor was 0.1, and the resolution of narrow regions was 1. It should be noted that in order to get an accurate result, the mesh element limits should be set to be the smallest of either 1/5 wavelength or the criterion that a layer should contain at least five mesh points in its 'thin' direction; however, in order to save computational time, the maximum element size was set to 0.1 mm and the minimum element size to 0.01 for frequencies lower than 2.9 MHz. For frequencies higher than 2.9 MHz, the maximum element size was 0.08 mm and the minimum element size 0.008. The model was solved with a direct solver.

2.3 Device Design, Fabrication, Assembly and Testing

The microfluidic channel layout was first designed in AutoCAD. Designs were transferred directly to photomasks for fabrication in 63.5 mm x 63.5 mm x 1.5 mm soda lime/chromium blanks precoated with positive photoresist (5300Å AZ1500; Telic Co.). Patterned features were etched to a depth of ~60 μm. Channels were enclosed via calcium-assisted glass-glass bonding or fusion bonding of two glass blanks. A 24 mm x 28 mm x 1.5 mm thick PZT-8 piezoelectric transducer (P880, American Piezoelectric) was clamped to the top side of the LSBAW chips using water as an acoustic coupling medium. LSBAW chip assemblies were placed in a custom stage insert of an inverted microscope for experimental observation of acoustic particle separation and enrichment.

2.3.1 Fabrication

An overview of the entire LSBAW fabrication process is provided in Figure 2.3. Our study used glass channels rather than silicon channels due to the low cost and easy accessibility of fabrication tools for glass devices. Silicon channels (anisotropically etched to yield vertical sidewalls) are preferred over glass channels (isotropically etched to yield rounded) (Figure 2.4); however, silicon etching was not available, and the trapping efficiency of glass channels is typically only 2-15% lower than that of silicon [47]. Therefore, glass was thought to be a suitable material for the LSBAW chips reported here.

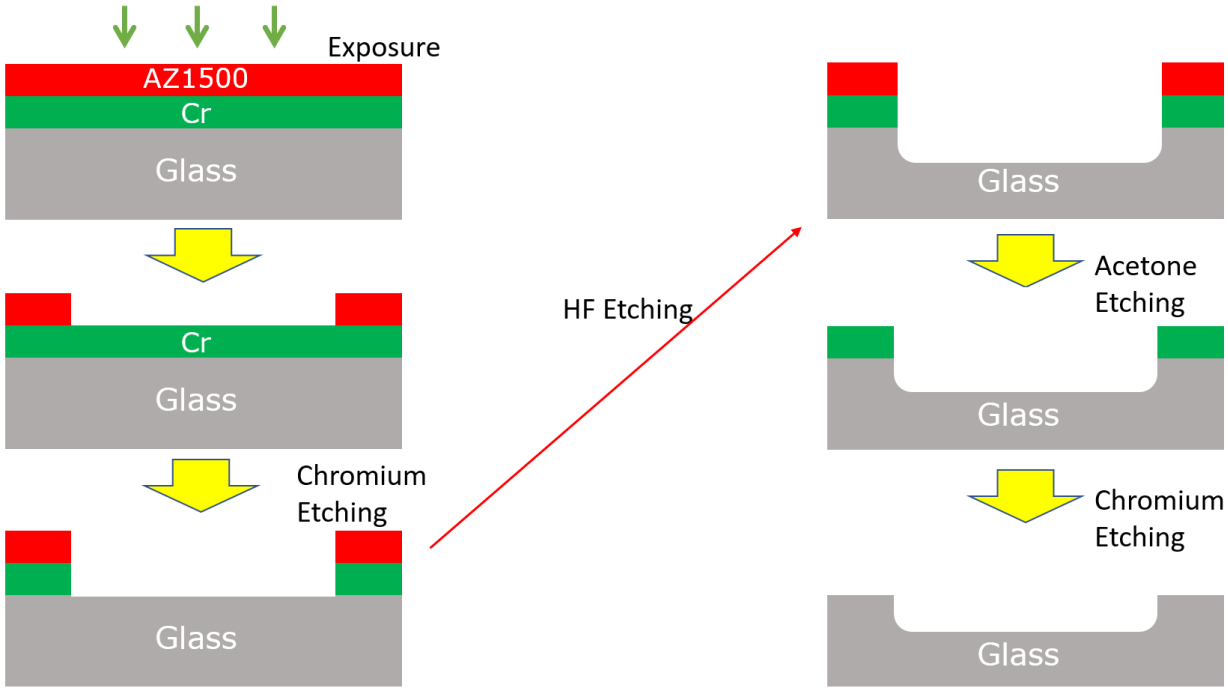

Figure 2.3 Etching process

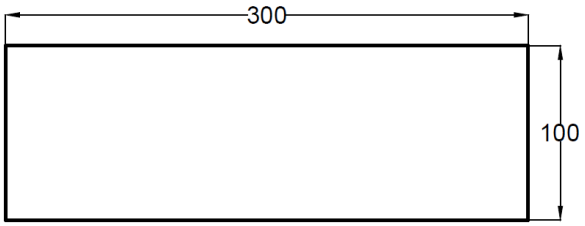

a) Cross-section of straight channel of etching on silicon channel

b) Cross-section of straight channel of etching on glass channel

Figure 2.4 Cross-section comparison of silicon and glass straight channel

Photolithography

After saving a microchannel layout as a .dxf file channel designs were directly written into the photoresist of a mask blank using a Heidelberg Laser Writing machine and the following parameters:

Table 2.1 Photolithography Parameters

Focus	-25%
Intensity	80%

Laser Power	47 mW
Filter	25%

The total exposure time for the 63.5 mm x 63.5 mm pattern was 50 minutes. Microchannel patterns were then transferred into the chromium layer in chromium etchant using the remaining photoresist as an etch mask. The total chromium etching time was about 1 minute, until the channel pattern appeared transparent (Figure 2.5).

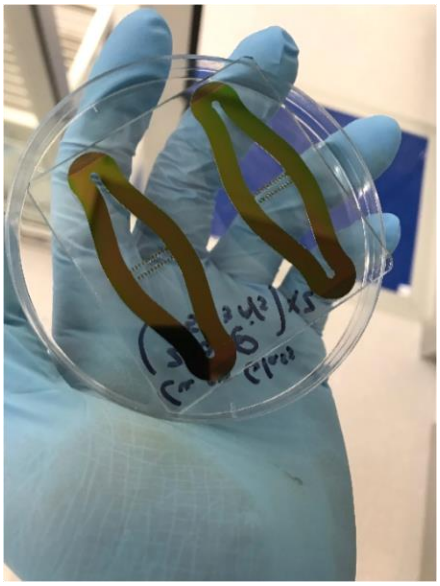

Figure 2.5 Channel geometry after chromium etching (refined LSBAW geometries)

Wet Etching

LSBAW microchannels were then etched into the glass blank using remaining photoresist and patterned chromium as an etch mask. Patterned features were etched to a depth of ~60 μm using 49% (w/w) HF:69% (w/w) HNO3: DI water at a ratio of 2:1:6. For our first two prototype channels, we performed a 14 minute etch (4 x 3 minutes of etching, followed by a 2-minute etch to the desired depth); after each step, blanks were rinsed in two water baths and dried using nitrogen to clear the channel of unwanted etch products (Figure 2.6(a)).

The same process was used to etch subsequent refined LSBAW channel geometries; however, it appears that the HF and HNO3 solutions were diluted during the etching process, as the etch depth for these chips was only 40 μm. Additional 3-minute and 1.5-minute etches were performed to reach a final depth of 54.8 μm (Figure 2.6(b)).

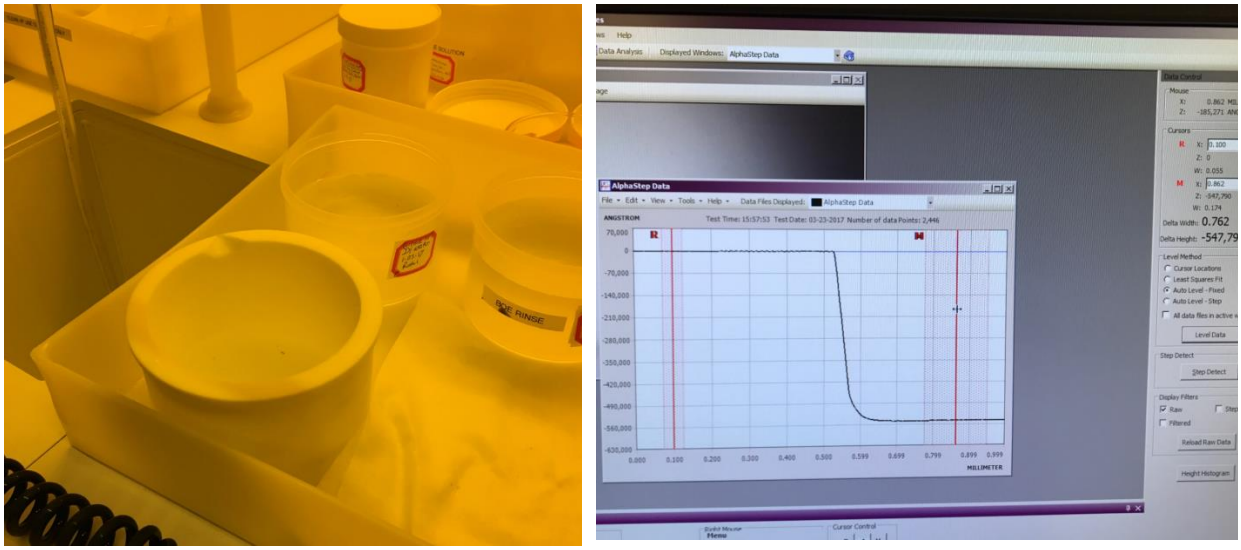

a) Etching Setup b) Depth Measurement

Figure 2.6 Etching process and depth measurement

Drilling and Dicing

Channel inlet and outlet holes were manually drilled using a high-speed micromotor (Espert 500, Nakanishi Co.) and a 1 mm diameter diamond drill bit. The drilling speed was 20,000 RPM. Channels were then sonicated for 2 minutes at 50 Hz to remove glass fragments (Figure 2.7). Finally, channels were thoroughly cleaned using Alconox. Each mask blank included two channel designs so the mask blanks were diced to yield individual channels (DAD 323, Disco).

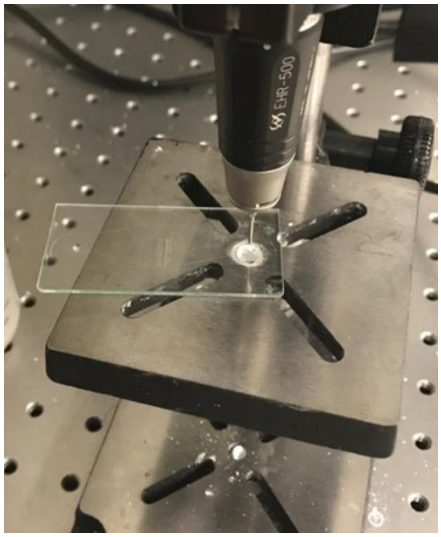

a) Drilling

b) Sonicating

Figure 2.7 Drilling and Sonicating

Glass Bonding

Glass channels were sealed with an additional mask blank either by calcium assisted bonding or fusion bonding. Fusion bonding is performed at high temperature using a heated press (Figure 2.8). Cartridge heaters were used to raise the temperature of the press blocks to 600°C, which is above the glass transition temperature of the soda lime mask blanks (580°C). The average bonding time used for each channel was approximately 30 hrs; however, due to surface imperfections following previous steps the two glass surfaces had some micro-roughness resulting in imperfect bonding. Though leaking was observed in some experiments, it is not thought to affect the conclusions of our investigations due to the static nature of the separation and enrichment conducted for this thesis.

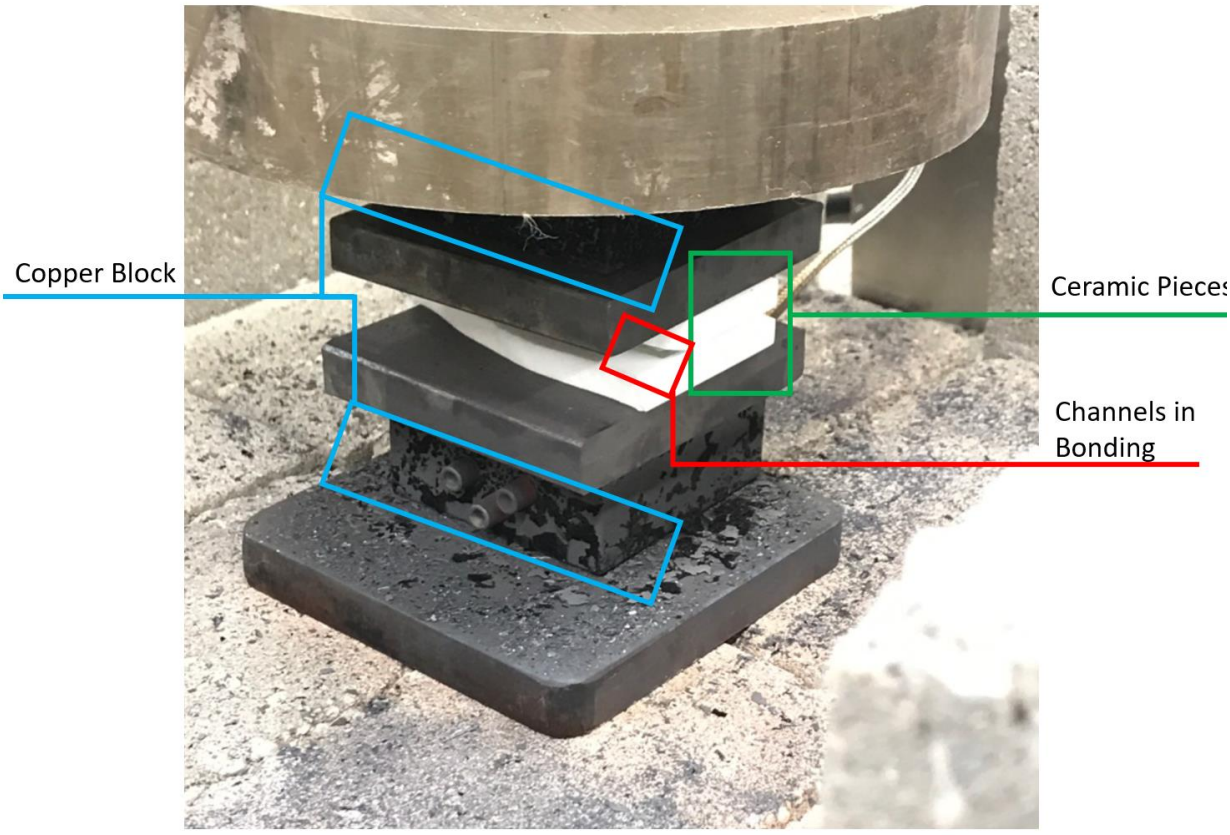

Figure 2.8 Bonding Setup

2.3.2 Experimental Setup and LSBAW Operation

Enrichment performance was evaluated using suspensions of polystyrene (PS) beads (5-µm and 20-µm diameter at concentrations of ~$2x10^6$ and ~$5x10^5$ beads per mL DI water, respectively; with density 1.06 g/cm^3; Phosphorex) and borosilicate hollow glass spheres (10 µm measured diameter, Dantec Dynamics) decorated with fluorescent polyclonal secondary antibodies (rabbit anti-goat IgG Alexa Fluor 488, Abcam), which were synthesized following a previously reported protocol [50, 51]. In addition, inlet and outlet compression ports were used for introduction of particle suspensions. LSBAW chip assemblies were placed in a custom stage insert of an inverted microscope (Axio Observer z.1, Zeiss) for observation of acoustic particle enrichment and terminal focusing. Enrichment frequencies were identified experimentally by sweeping transducer actuation over a 50kHz range about predicted resonances of interest (33522A,

Agilent; 2100L, ENI). Two piezoelectric configurations were used for the different LSBAW chips. For initial prototype chips, the transducer was clamped to the top of the channel using a thin layer of DI water for acoustic coupling (Figure 2.9). For refined LSBAW geometries, the piezoelectric was placed either on a lateral side (Figure 2.10) or on the bottom side of the chip as it was found that the position of the piezoelectric had little impact on observed particle focusing shapes.

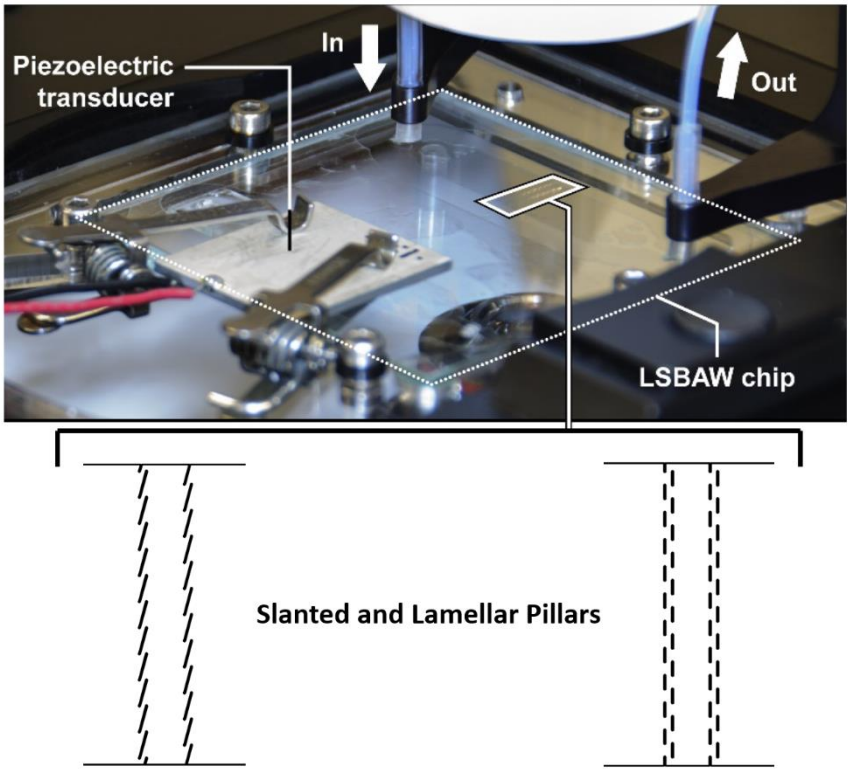

Figure 2.9 Experimental setup: The piezoelectric actuated the glass chip from the top surface with a thin layer of DI water for acoustic coupling. The 10 mm wide LSBAW slanted and lamellar channels were etched in the same glass chip shown in this figure.

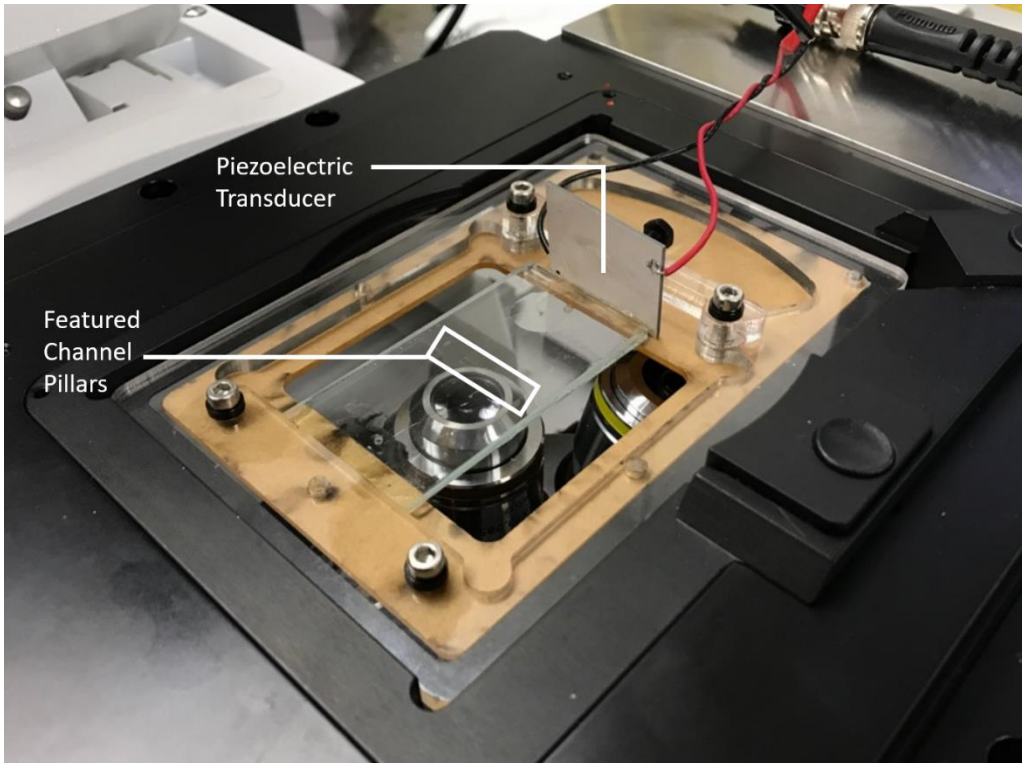

Figure 2.10 Experiment setup: The piezoelectric actuated the glass chip from a lateral side

2.4 Summary of Theory and Methods

In this chapter, we introduced the acoustofluidic theory that underlies longitudinal standing bulk acoustic wave (LSBAW) microparticle separation and enrichment. Numerical methods used for design and predictive modeling of LSBAW architectures were then described. After several assumptions and simplifications, a 2D model was developed to determine eigenfrequencies and eigenmodes of the LSBAW microchannels. The 2D model provides a qualitative description of the mechanisms responsible for particle separation and enrichment in these devices, and accurately predicts their experimentally observed behavior (see Chapter 3). Lastly, fabrication, assembly and experimental methods used to evaluate enrichment performance of LSBAW chips were presented.

Chapter 3: Performance of the Initial LSBAW Microfluidic Channels

In this chapter, we show model predictions and experimental results for a set of preliminary LSBAW microfluidic channels. Eigenfrequency analyses were used to identify potential operating frequencies for particle focusing, and realized devices were actuated near those frequencies to identify optimal particle trapping conditions. Observed performance is compared to that of an ideal particle separator, which would provide robust, selective trapping of targeted particles in the enrichment zone. In this context, each design is assessed and possible optimization strategies for future LSBAW channel designs are presented.

3.1 Introduction

In this section, we briefly introduce the general theory of LSBAW focusing and the geometry of the four initial LSBAW channels.

3.1.1 Mechanisms Underlying LSBAW Operation

For an ideal rectangular microchannel under the actuation of an ultrasound transducer (e.g., a piezoelectric element), the side walls of the channel vibrate such that the wall boundaries of the enclosed fluid can be considered free. Antinodes are thus found at the walls. The simplest standing wave under these circumstances features a single node at the channel midline, which is called the first half wavelength resonance or the first mode. When a wave is established such that two nodes separated by an antinode are located within the channel cross-section that is the second mode, and so on. Figure 3.1 illustrates the structures of the 1^{st} to 5^{th} modes for a simple straight channel geometry. In addition, given the width of the channel w, one can approximate a resonant frequency with the below formula:

$$f \approx \frac{nc}{2w} \tag{16}$$

where c is the speed of sound in the medium, n is the mode number, and f is the driving frequency that generates the corresponding mode. A thorough discussion of simple channel design optimization is provided by Glynne-Jones et al. [52].

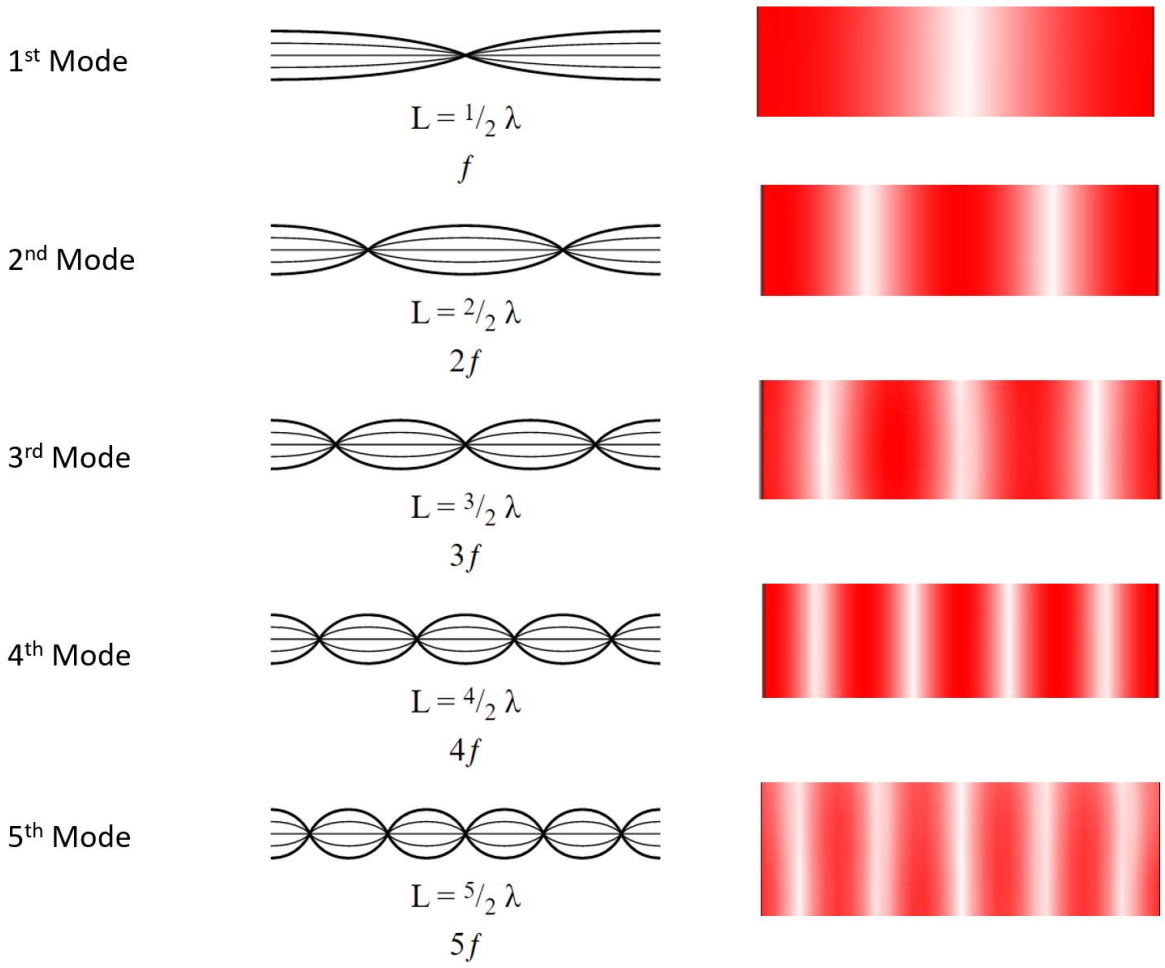

Figure 3.1 Mode illustration: (a) mode number, (b) illustration of corresponding ultrasonic standing wave, and (c) depiction of pressure field between straight channel walls with red denoting areas of high pressure and white denoting areas of zero pressure.

In our present work, we introduce 'pseudo walls' that support a pressure field to trap and separate particles of varying compositions and sizes without obstructing flow in the axial direction. For positive acoustic contrast particles with diameters greater than a critical threshold,

the acoustic radiation force will dominate over Stokes' drag causing particle retention, while particles below this threshold will remain in flow (Figure 3.2). Therefore, several parameters were manipulated to effectively enhance the local pressure field between the pillar arrays to increase separation capability.

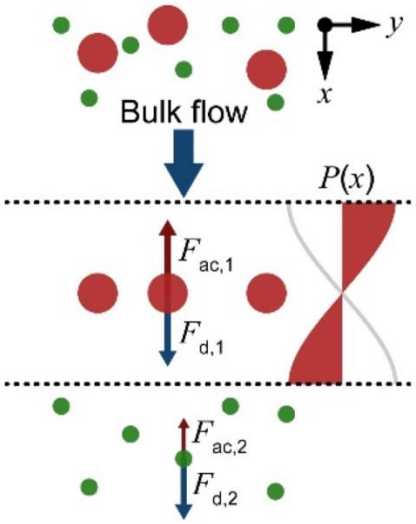

Figure 3.2 Illustration of particle trapping from bulk flow using an LSBAW channel. The large red particles exemplify beads that are above the critical threshold for acoustic radiation forces to overcome Stokes' drag and are therefore held in the acoustic trap, while drag dominates for the green particles that remain in fluid flow.

3.1.2 The Geometry of Four Initial LSBAW Channels

The geometries of our initial four channels are shown in Figure 3.3. We have named the pillar geometries in Figure 3.3 (a) 'slanted' and those in Figure 3.3 (b) 'lamellar'. For the channels shown in Figure 3.3, the overall length is 50 mm and the width is 4.67 mm. The pillar configurations of the initial channels were designed to maintain a first half-wave resonance at approximately 500 kHz (i.e., to match a range of piezoelectric driving frequencies from 500 kHz to 2.5 MHz to actuate the first five device modes). This design consideration corresponds to pillar array gaps between 1.2 mm and 1.5 mm as explained in Section 3.1.1.

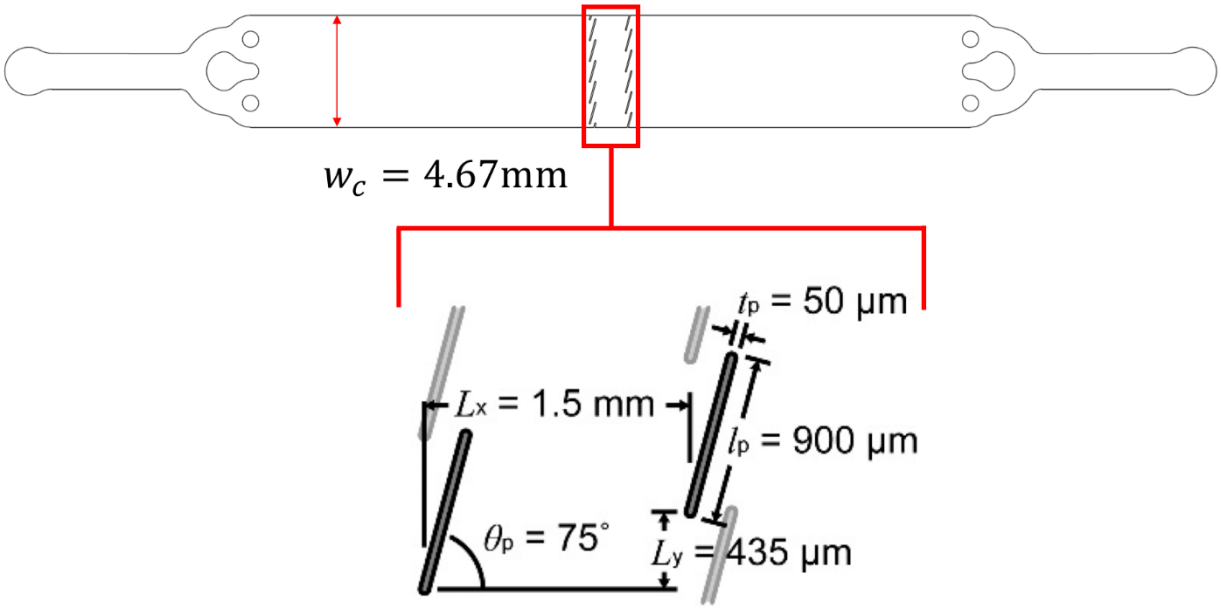

(a) 4.67 mm slanted LSBAW geometry

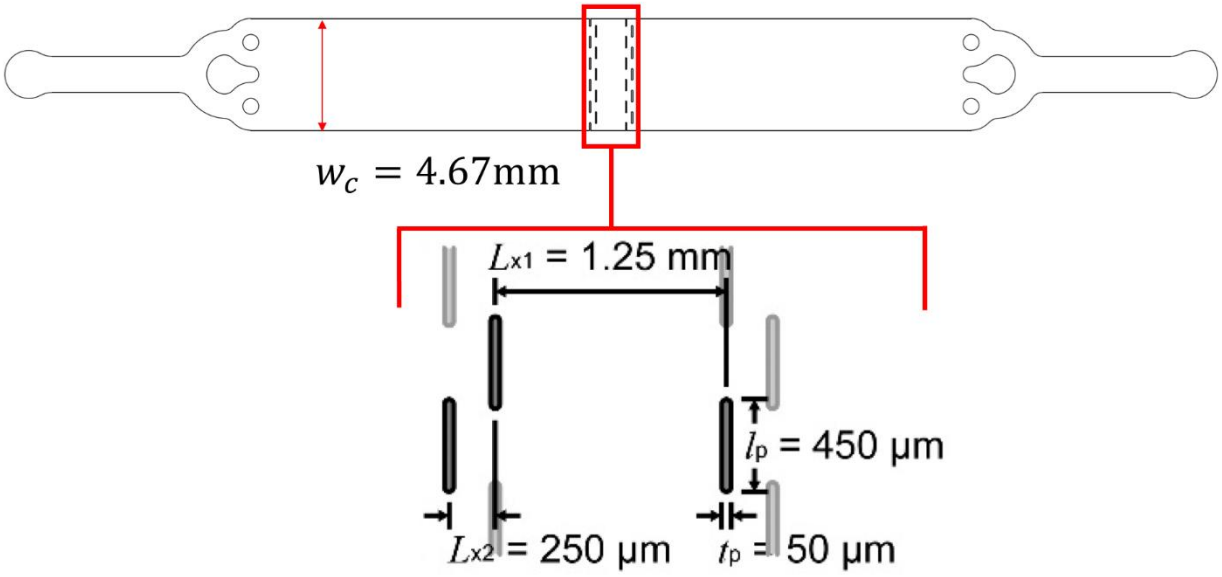

(b) 4.67 mm lamellar LSBAW geometry

Figure 3.3 4.67 mm wide LSBAW straight channel

We also designed channels with slanted and lamellar pillars where the channel width was extended to 10 mm and the inlet/outlet regions were altered to accommodate the effective

increase in cross-sectional area. Otherwise, the basic geometry of the pillar arrays remained unchanged (see Figure 3.4).

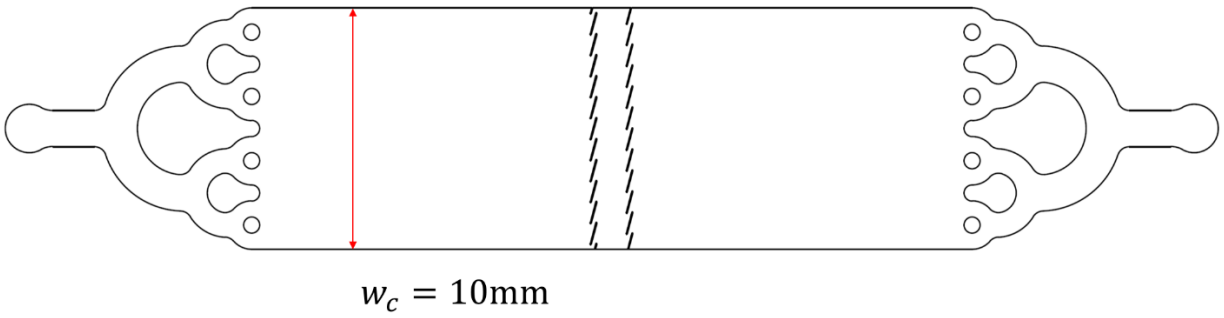

(a) 10 mm slanted LSBAW geometry

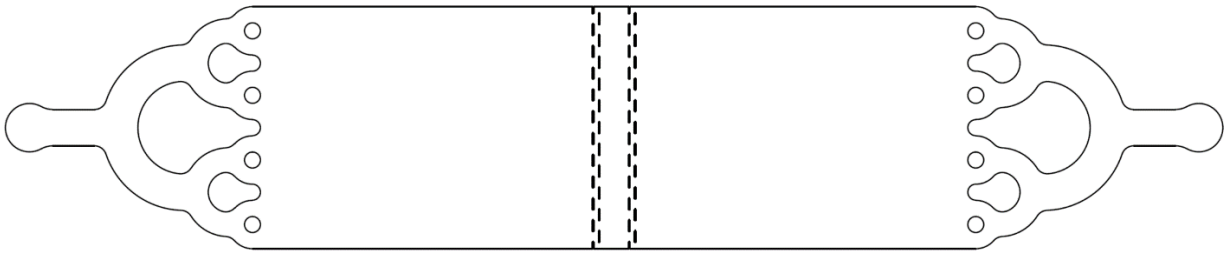

(b) 10 mm lamellar LSBAW geometry

Figure 3.4 10 mm wide LSBAW straight channel

3.2 Results and Discussion

Because several effects are neglected (e.g., the influence of the actuator/resonator and fluid viscosity), modal analyses provide only a qualitative description of the trapping potential of a given LSBAW architecture. In addition, the nature of the isotropic glass etch forms inherently three-dimensional (3D) pillars that are represented in only two dimensions. Thus, the resultant variability of the width as a function of height is neglected, which can cause device resonances to deviate from predicted higher harmonics of the fundamental frequency [47].

Nevertheless, the 2D model is thought to provide the best balance of accuracy and computational expense. To identify possible resonant frequencies, eigenfrequency analysis was performed in

the four flow channels with a frequency envelope of 500 kHz to 2.8 MHz. Though the 2D eigenfrequency analyses can only qualitatively describe the pressure field shape, they still allow for prediction of the resonant frequencies by comparing the pressure amplitude ratio or acoustic energy density ratio of the enrichment region to that of the inlet/outlet region (Figure 3.5).

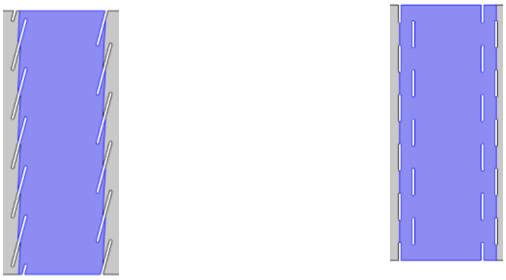

(a) Illustration of the enrichment region

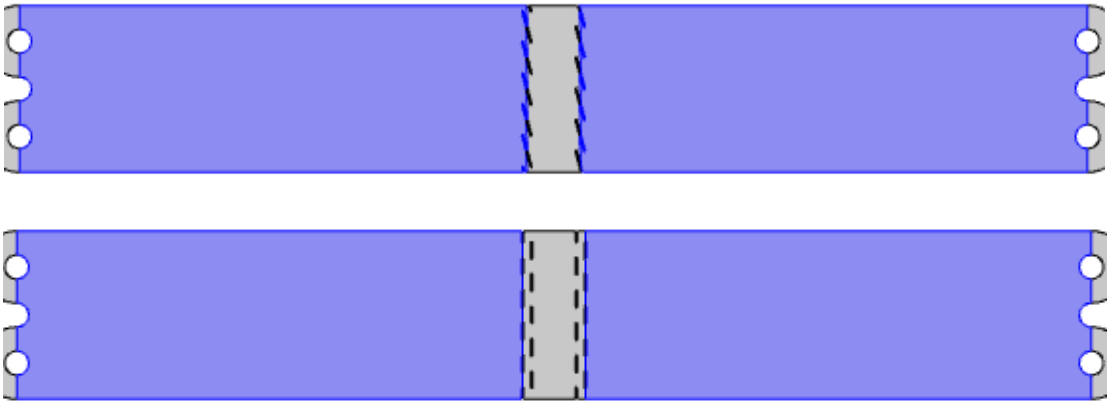

(b) Illustration of the inlet and outlet region

Figure 3.5 Acoustic energy density ratio regions: (a) illustration of the enrichment region (b) illustration of the inlet and outlet region

Acoustic energy density comprises a kinetic and a potential energy, which are written as:

$$E_{ac} = \frac{1}{4\rho_w}\left[\frac{|\nabla p|^2}{\omega^2} + \frac{p^2}{c_w^2}\right] \tag{17}$$

The angular frequency is represented in the equation as ω [59]. From the equation, the E_{ac} is proportional to the square of the gradient of the pressure and the square of pressure amplitude.

Critical frequencies are shown as local peaks in the plots of the E_{ac} ratio sweep of the 4.67 mm wide channel as shown in Figure 3.6. From these two E_{ac} ratio plots, the peak points (frequencies where the acoustic energy in the enrichment region is higher than outer region) were selected as candidates for particle trapping. However, the formed pressure fields may not be conducive to retention under flow due to non-orthogonal and non-linear banding. Therefore, plots of the potential pressure fields of these peaks are shown in Figure 3.7.

For the slanted channel, the only applicable pressure field capable of particle trapping and separation was found at 0.579 MHz. At 1.053 MHz (the second mode), the pressure field does not visually appear to properly form zero pressure nodes perpendicular to the direction of the flow for the length of the pillar array, and thus the particles might flow away along longitudinal zero pressure nodes driven by the drag. For the lamellar channel, we found that 0.584 MHz, 1.385 MHz and 2.469 MHz produced pressure fields that visually have the proper attributes for effective trapping and separation.

A common similarity between the slanted and lamellar array geometries is that for possible resonances greater than the first mode, there appears to be deviation from ideal pressure banding due to the presence of lateral resonances. This is most notable for frequencies greater than 1 MHz where the pressure field takes on a waviness that would not be seen in an ideal straight-walled geometry.

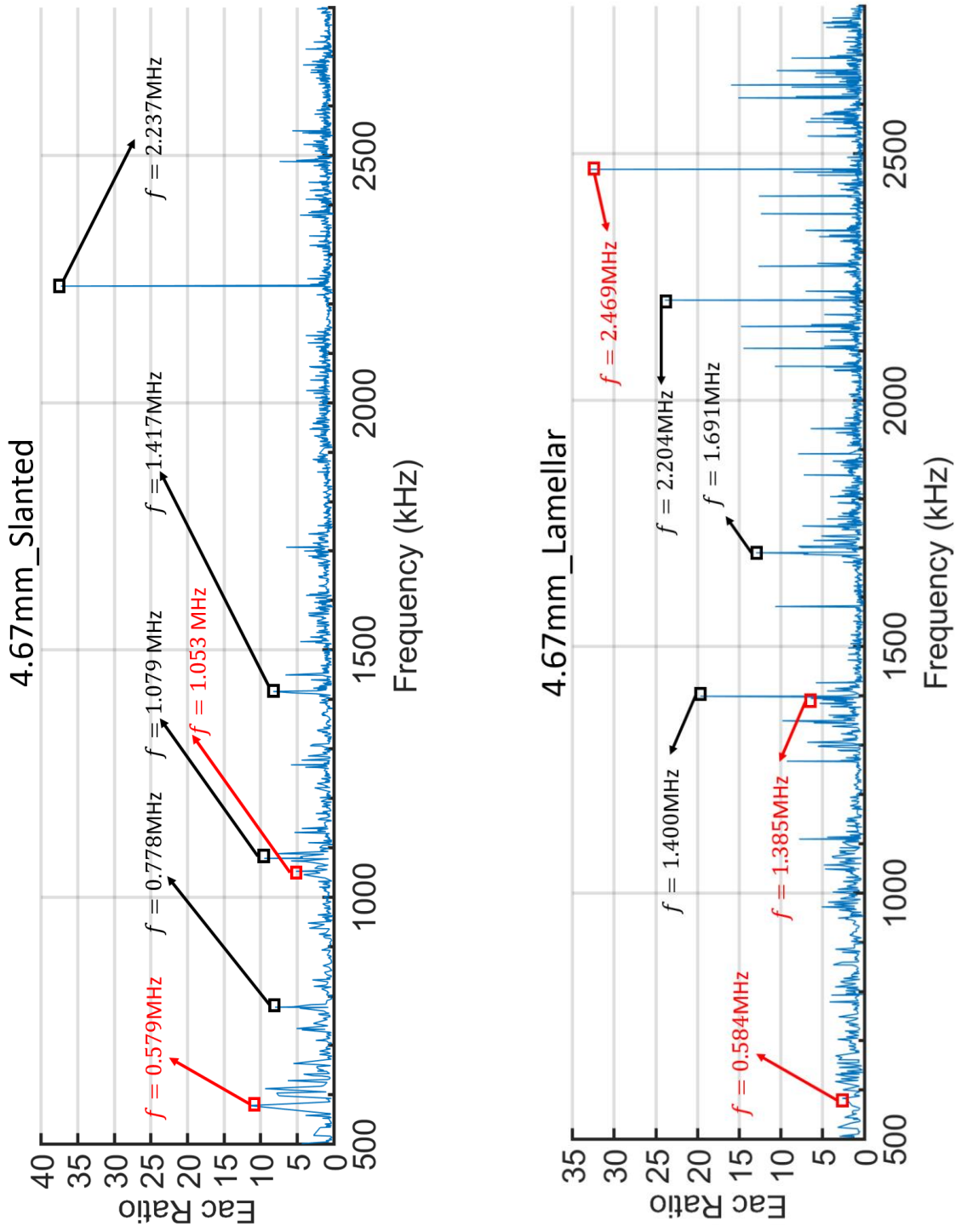

Figure 3.6 Acoustic energy density ratio sweep of 4.67 mm wide LSBAW slanted and lamellar channels

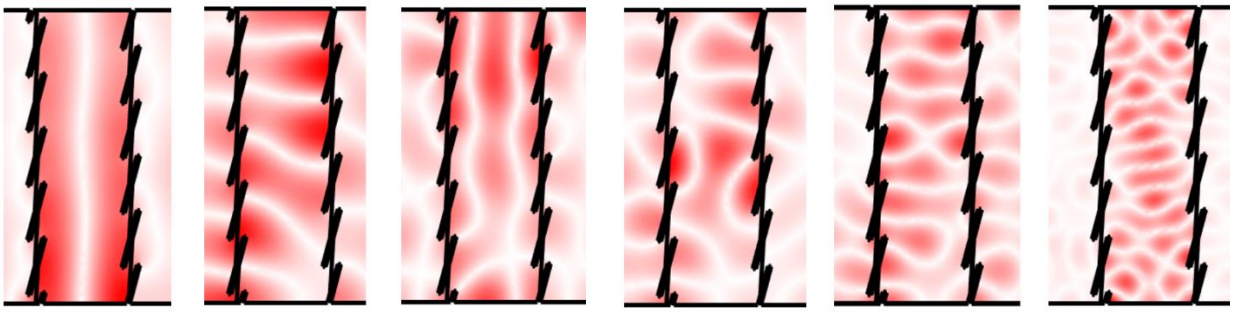

0.579 MHz 0.778 MHz 1.053 MHz 1.079 MHz 1.417 MHz 2.237 MHz

(a) 4.67 mm wide LSBAW slanted channel simulation results

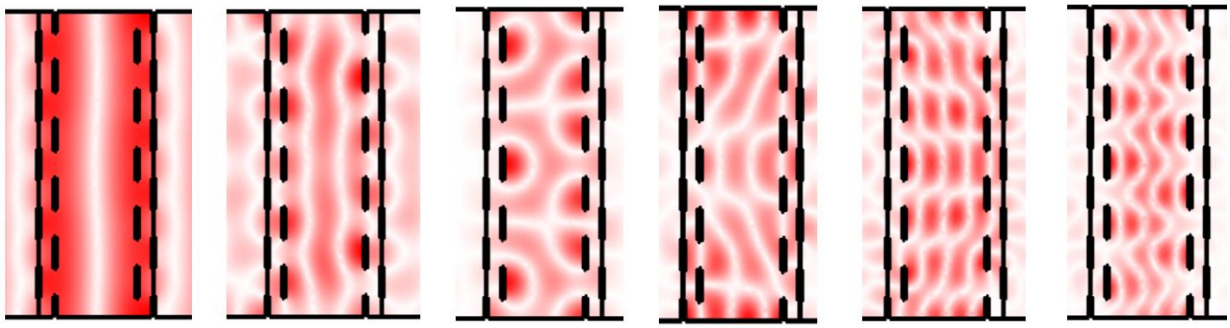

0.584 MHz ***1.385 MHz*** 1.400 MHz 1.691 MHz 2.204 MHz **2.469 MHz**

(b) 4.67 mm wide LSBAW lamellar channel simulation results

Figure 3.7 Pressure fields of slanted and lamellar channels. The bold red in the enrichment area stands for high pressure amplitude, which is generated by the pillars. The light red in the inlet and outlet area stands for lower pressure amplitude compared to the pressure amplitude in the enrichment area.

Predicted mode shapes and frequencies were used to guide and assess the terminal particle distribution, defined as the state of no motion in the direction of a node or an antinode of the acoustic field, for polystyrene (PS) beads (Figure 3.8 (a)) and fluorescent glass beads (Figure 3.8 (b)). Results showed remarkable similarity between the modeled zero pressure regions and experimental 20 μm bead locations, as both particle types exhibit positive acoustic contrast and should focus to the nodes of the field (see Figure 3.8). However, 5 μm beads were unaffected by the acoustic field. These results demonstrate the efficacy of field amplification by 'pseudo walls'

for preferential immobilization of 10-20 μm particles from fluids and other objects of sub-critical diameter.

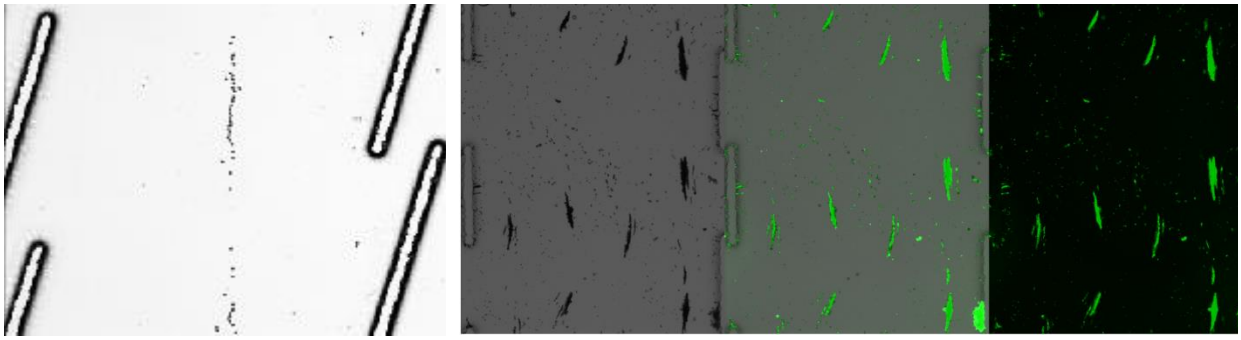

a) 0.57 MHz b) 2.45 MHz

Figure 3.8 Focusing experiments (a) focusing of 20 μm PS beads from 5 μm PS beads (b) focusing of fluorescent antibody-decorated glass spheres

After qualitative model validation, the predicted E_{ac} ratio was used to demonstrate that the local pressure field within the pillar array is enhanced by the inclusion of the slanted and lamellar features. For the slanted pillar channel, the E_{ac} ratio at 0.579 MHz is 11.6. If the acoustic energy ratio at a frequency is greater than 1, operation at this frequency should be suitable for acoustic trapping. For the lamellar channel, the E_{ac} ratio for 0.584 MHz is 2.6, while the E_{ac} ratio for 2.469 MHz is 32. This higher frequency provided the largest amplification of all modeled cases. Experimentally-determined resonances, found at 0.57 MHz and 2.45 MHz, varied slightly from the predicted resonances of 0.584 MHz and 2.469 MHz for the first and fourth modes, respectively. For the slanted pillar channel, it was also noted that varying the driving frequency slightly (±10 kHz) from the observed resonant frequency resulted in a change in the pressure field shape. This suggests that the harmonic response of this channel is potentially too sensitive for real world operation where properties of the fluid (speed of sound) and resonator can change due to actuator heat generation or changes in ambient room temperature. Plots of the E_{ac} sweeps of the 10 mm wide LSBAW channels are shown in Figure 3.9.

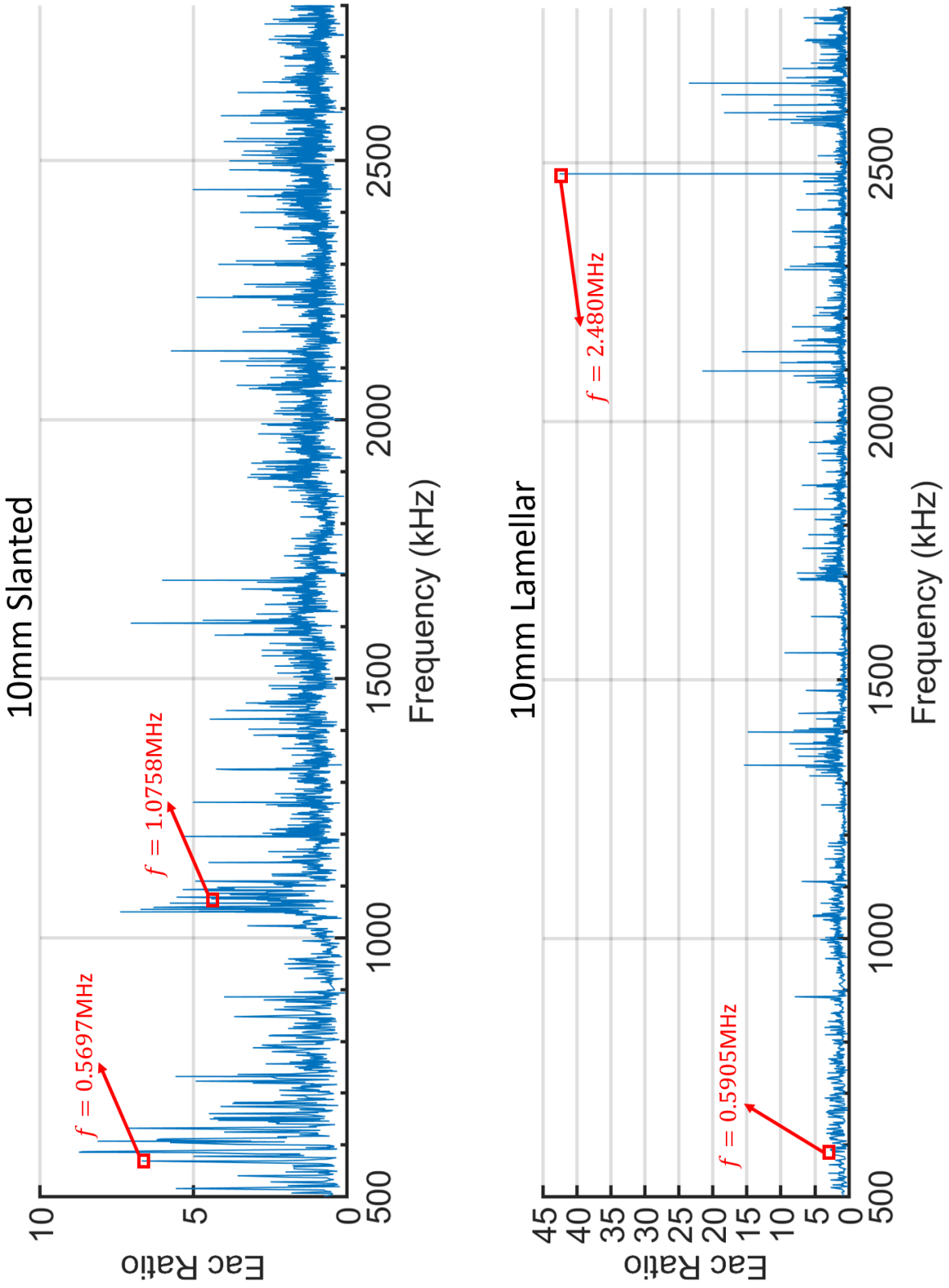

Figure 3.9 Acoustic energy density ratio sweep of 10 mm slanted and lamellar channels

The predicted first and second modes for the slanted 10 mm channel are 0.5697 MHz and 1.0758 MHz, with corresponding E_{ac} ratios of 6.67 and 4.41, respectively. For the lamellar device, the first and fourth mode driving frequencies are 0.5905 MHz and 2.480 MHz, with E_{ac} ratio of 2.61 and 42.53, respectively.

Again, model predictions were used to guide experimental assessment of each channel. For the 10 mm slanted channel, model and experimental results for the first mode are shown in Figure 3.10 (a). The predicted pressure field in the simulation exhibits a remarkable similarity to the observed particle distribution found between 0.57 MHz and 0.575 MHz. Experimentally, the 10 mm LSBAW channel produced a more robust operation with small deviations in driving frequencies resulting in little or no change to the terminal particle distribution, which contrasts the behavior of the 4.67 mm LSBAW channel.

For the 10 mm lamellar channel, we also found the first mode experimentally as shown in Figure 3.10 (b). The range of frequencies found for the first mode of the experiment was 0.57-0.575 MHz, about 0.015-0.02 MHz off the predicted 0.59 MHz. Future work needs to be done on these two 10 mm chips to optimize their operation under flow rates, i.e. finding higher frequency modes, quantitatively assessing the sensitivity and specificity of the particle retention, etc.

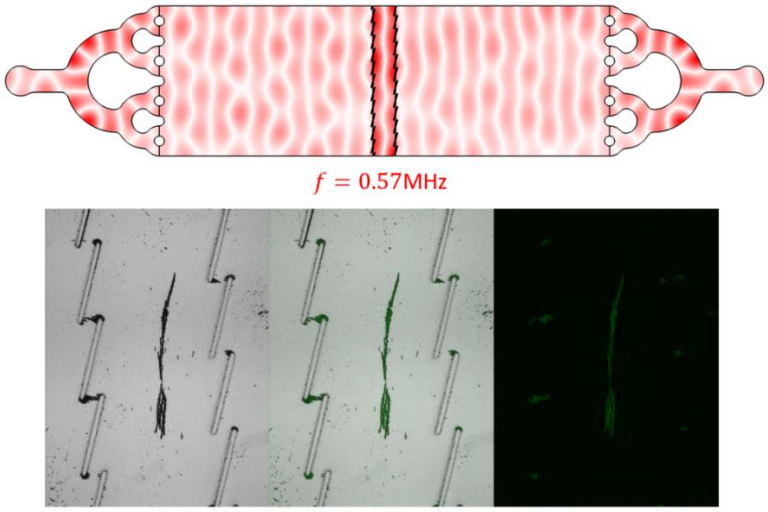

(a) First mode of 10 mm wide LSBAW slanted channel

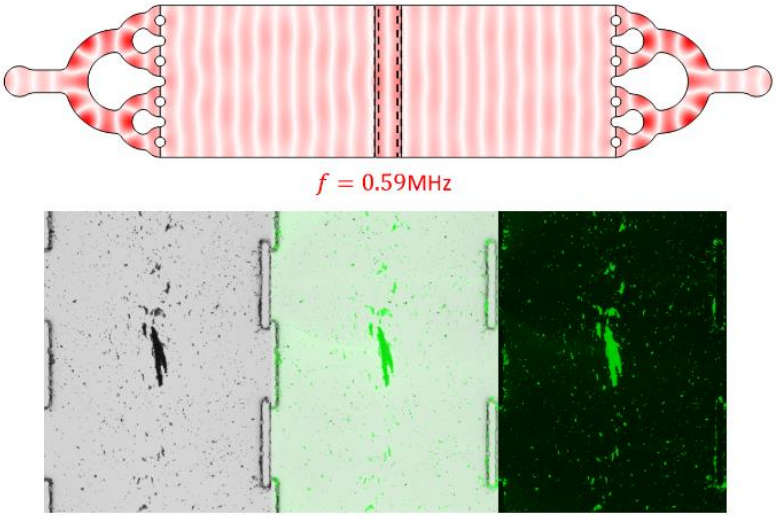

(b) First mode of 10 mm wide LSBAW lamellar channel

Figure 3.10 First mode of 10 mm wide LSBAW channels simulation results and experimental results with fluorescent antibody-decorated glass spheres

3.3 Conclusions

Experimental results for initial LSBAW microchannels demonstrate field amplification by 'pseudo walls' for preferential immobilization of 20 μm PS particles from 5 μm PS particles, as well as focusing of 10 μm fluorescent hollow glass spheres under static (no-flow) conditions. The LSBAW architectures also permit continuous flow purification of particles above a critical

diameter for frequencies with high field amplification. However, the resonant frequencies and pressure fields we have in these four channels are not ideal and not optimized for this purpose. From these initial observations, there are several aspects that could be improved, some of which are detailed below.

3.1.1 Lateral Resonant Mode Effects

The pressure field in the predefined enrichment region is sensitive to experimental conditions causing difficulty forming a stable trapping pattern. One can easily see that the channel width also affects the pressure field (Figure 3.7). Because of this, we were unable to find a stable second mode in both the simulation and experiment. The non-linear and disrupted longitudinal resonant modes were caused by interference from lateral resonant modes. This is due to the channel width and the inter-pillar distance both being of millimeter dimensions, allowing for resonant frequency overlap as verified both computationally and experimentally.

In addition, the narrow width of the channel limits the throughput of the device. In many particle enrichment and separation applications, there is a need to process relatively larger volumes of solutions. To accomplish this while keeping the depth of the channel unchanged, the width of channel can be increased to achieve an increase in the volumetric flow rate.

3.1.2 Influence of Pillar Thickness

The pillars in our case can be considered thin with a width of only 50 μm, while the wavelengths of operation for the device range from 500 μm (3 MHz) to 3000 μm (0.5 MHz). The low amplitude of the standing pressure field between the pillars is in part due to this thin resonator loss as the pillars are incapable of acting as perfect reflectors and instead allow propagation of the acoustic waves through the feature. Therefore, a possible improvement in overall LSBAW

design involves increasing the thickness of the pillars so they are well above the critical thickness of one-tenth the wavelength of the ultrasound.

3.1.3 Streaming Effects

Dual et al. [54] reported a novel acoustophoretic cell trapping method on oscillating sharp-edged structures that protrude into a microfluidic channel. These structures were found to trap cells and particles reliably using simple piezoelectric excitation. The oscillating sharp edges generate an acoustic field around their tips, which can trap particles regardless the geometric dimensions or operating frequency (a precise resonant frequency is not required). In our experiments, we observe a similar effect whereby streaming flow appears to cause particle trapping at the pillar surfaces. This phenomenon might limit the capability for trapping; however, under flow conditions at optimal trapping frequencies, we expect this effect to be minimal.

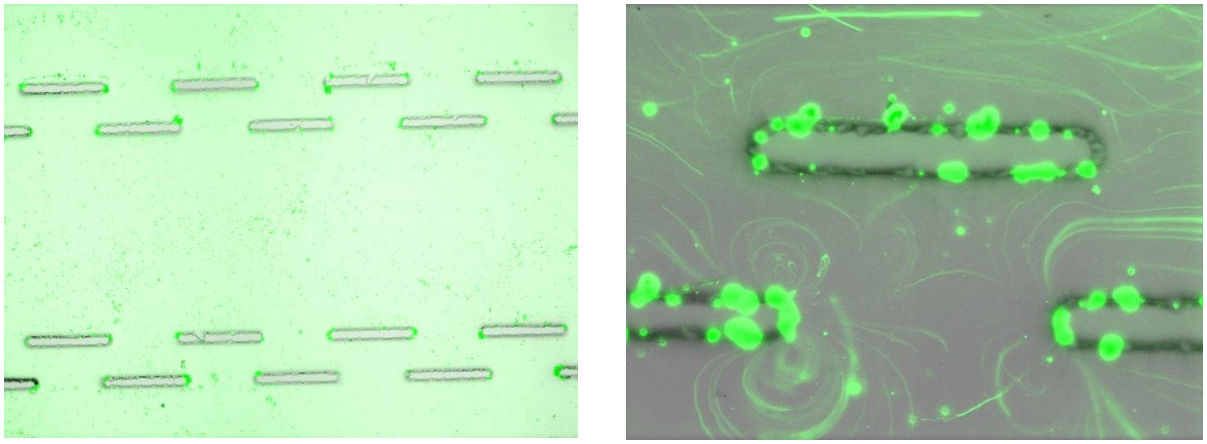

a) Sharp edge focusing

b) Sharp edge acoustic streaming

Figure 3.11 Sharp edge effects

Chapter 4: Potential LSBAW Microfluidic Channel Improvements

In Chapter 3, we identified several areas for potential improvement of the LSBAW microfluidic channel platform. Here, we present device modifications that are meant to address each of those shortcomings.

4.1 Introduction of Tapered Channels with Thicker Pillars

We modified the channel and pillar geometries to address the problems observed during experimental evaluation of initial LSBAW prototypes. To eliminate focusing in the inlet and outlet regions, we incorporated tapered channels, which induce a higher flow velocity and are not as prone to development of lateral standing waves. We also thickened the pillars to strengthen the pressure field in the enrichment area. The two new channel geometries are shown in Figure 4.1.

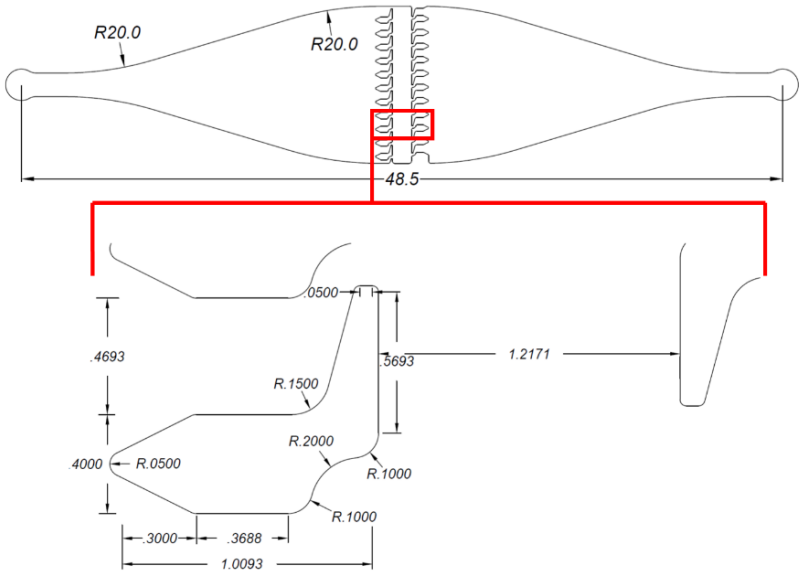

(a) 10 mm wide LSBAW tapered channel 1

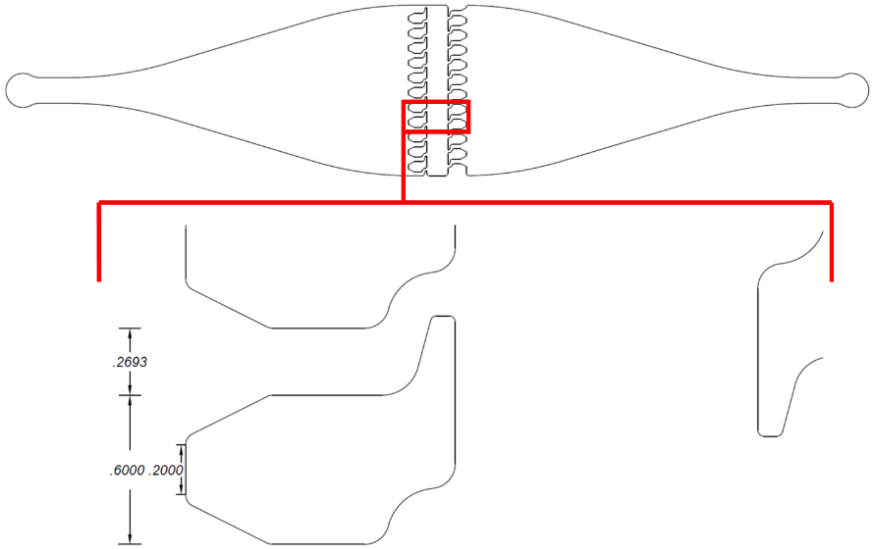

(b) 10 mm wide LSBAW tapered channel 2

Figure 4.1 10 mm wide LSBAW tapered channels with thicker pillars

The new pillar and microchannel designs are meant to address previously identified areas for improvement in the following ways:

1) For initial prototypes, we observed that the 10 mm width channels have more stable performance than the 4.67 mm width ones, likely because the lateral ultrasonic standing waves have less influence on the pressure field for wider channels. Therefore, we chose 10 mm for the channel width of refined devices.
2) We made pillars thicker in the both lateral and longitudinal directions to strengthen the pressure amplitude inside the enrichment area; however, due to the isotropic glass etching process, the gap between each pillar must be at least 200 μm.
3) To avoid trapping particles at the edges of the pillars, we enlarged the thinnest part of the new pillars to 100 μm. Dual has shown that particles trap at sharp edges; however, almost no trapping was observed when the pillar dimensions were at least 100 μm [54]. While it is unlikely that trapping by this mechanism would occur under typical operating

conditions (i.e., frequencies at which focusing and enrichment occur within the enrichment area), altering the pillar geometry in this way provides additional insurance against such adverse phenomena.

4) We used lamellar-like pillars since the lamellar pillars provided more consistent trapping in initial prototype devices.

4.2 Results and Discussion

The acoustic energy density versus frequency sweeps for both refined LSBAW geometries are shown in Figure 4.2. As before, we investigated the pressure field mode shapes around possible resonant frequencies, selecting five frequencies of operation for the first tapered channel and two for the second (Figure 4.3). Acoustic fields with desired shapes (straight vertical lines within the enrichment area) did not occur at the highest E_{ac} ratio peaks, and in fact performance as assessed using this method suggests that initial prototype geometries may provide better enrichment than refined geometries. The E_{ac} ratios for the identified frequencies are 3.94, 1.92, 1.72, 0.79, and 1.07 for the first channel and 1.62 and 2.00 for the second. These ratios are generally lower than those for the straight channels discussed in the last chapter. Note that the vast majority of larger peaks in E_{ac} ratio represent frequencies at which lateral banding within the enrichment area dominates the field, precisely the behavior that we were attempting to avoid.

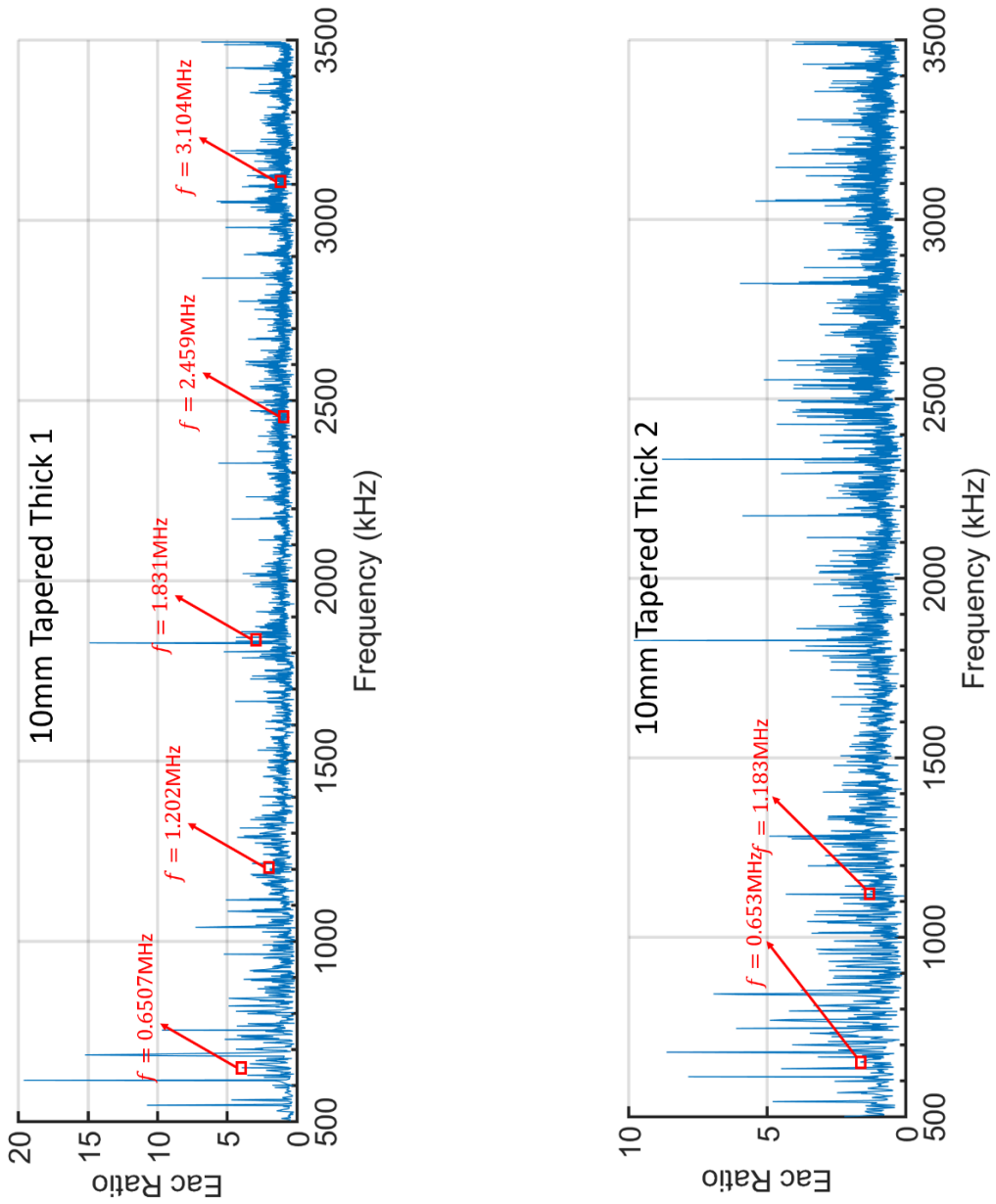

Figure 4.2 Acoustic energy density ratio sweep of tapered channel

For LSBAW tapered channel 1, the first mode in experiments matched the simulation results very well; however, only a slight adjustment of the driving frequency resulted in a significant change in the pressure field shape. The second mode was even more sensitive, and we were not able to find a frequency which could successfully trap particles. The third mode demonstrated the best experimental result with straight bands of particles, which were not sensitive to

frequency change. Unlike most of our results, the experimentally identified frequency for this case deviated 0.16 MHz (10%) from the simulated frequency. The fourth mode and the fifth mode in the experiments matched the predicted pressure field and resonant frequencies, but the pressure fields of both modes suggest a lateral amplitude distribution because the terminal mode shapes exhibit agglomeration of particles.

For LSBAW tapered channel 2, we located the first and second modes before the glass chip was broken. Though the first mode was sensitive to frequency change, the frequency and shape found experimentally matched model predictions. The second mode showed two clear vertical lines of particles trapped with few disconnected regions of particle agglomeration. Compared to the second mode for LSBAW tapered channel 1, it exhibited better trapping.

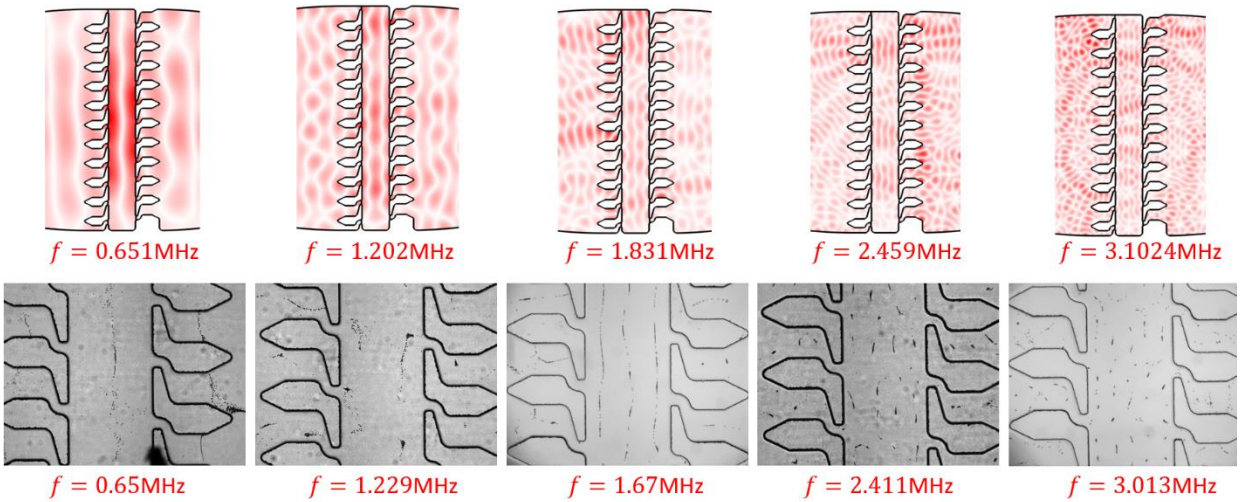

(a) 10 mm LSBAW tapered channel 1

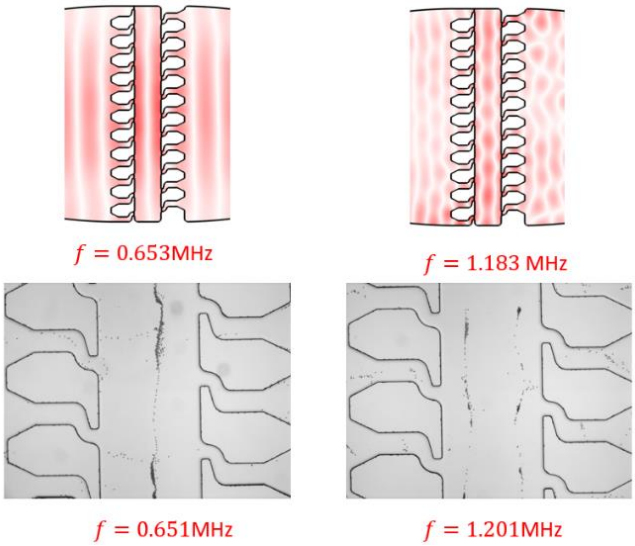

(b) 10mm LSBAW tapered channel 2

Figure 4.3 Resonant modes in model and experiment

4.3 Conclusions

In this chapter, we discussed the simulation and experimental evaluation of two refined LSBAW microfluidic channels. In these channels, the inlet and outlet regions were tapered and the pillar geometry was modified in an attempt to trap particles more efficiently in the enrichment region. The two channels have same dimensions, but different pillar thicknesses. We first studied the acoustic pressure fields in the two channels using COMSOL. We located five resonant frequencies with vertical zero pressure nodal lines in the enrichment area for the first channel, and two for the second channel. In experiments, we found the corresponding frequencies and successfully trapped particles in various modes. Of all cases reported in this thesis, higher modes for the tapered channels were least sensitive to frequency change; however, for the best particle trapping case (third half-wave resonance, LSBAW tapered channel 1, f = 1.67 MHz), the frequency of operation observed experimentally did not accurately match the model prediction.

The E_{ac} ratios predicted by the model were lower than those for the initial prototype straight channels. We modified the pillar and channel geometries to improve the trapping efficiency, yet

the results were not as expected. Prediction of the focusing and enrichment behavior of these complex geometries is not intuitive suggesting that a rigorous optimization study is needed to find optimal channel and pillar dimensions/shapes in a more systematic way. Once we have identified the optimal geometry for this type of channel, experiments under desired high flow rate (versus current static flow) should be done to test if these LSBAW microfluidic channels are suitable for real-life applications.

Chapter 5: Summary

We designed and fabricated six microfluidic channels with different inlet/outlet geometries and pillar shapes. The first four have straight channels with thin pillars. Two additional channels, with tapered inlet/outlet regions and thick pillars, were investigated to improve the trapping performance. Each of these designs demonstrated the pressure field amplification generated by 'pseudo walls.' This was shown via numerical studies in COMSOL and was also proven experimentally by trapping polystyrene beads (5 μm and 20 μm) and fluorescent hollow glass spheres (measured 10 μm) in a static fluid at a predefined channel location between two rows of pillars.

In general for LSBAW channels with simple lamellar and slanted pillars, particle trapping can be observed along the minimum pressure bands oriented perpendicular to the inflow direction. Though the dimensions of the pillars are relatively thin compared to the ultrasound wavelength, the 'pseudo walls' generate an acoustic field which is suitable to immobilize suspended particles using acoustic radiation forces enhanced by additional augmentation. Enhanced pressure fields were observed in both the numerical models and the experiments at predicted resonant frequencies. The simulation results also accurately predicted the resonant frequencies in experiments.

The two tapered channels with thick pillars were also able to trap particles in the enrichment region. The resonant frequencies were first found via numerical study and were proven in experiments; however, the experimental results exhibited some deviations from the simulation and the Eac ratios calculated were not as high as for the initial prototype straight channels.

To improve the performance of the LSBAW microfluidic channels, we plan on doing the following work in the future.

1) A more accurate model will be developed. We are in the process of adding glass and the piezoelectric transducer to our model, which will better represent our experimental setup. A 3D model will provide more precise simulations, though we must also investigate a way to minimize the computational cost.
2) An optimization study will be performed to identify the geometry of channels and pillars, which would provide the best trapping efficiency.
3) Though the glass etching is a low-cost method, it lacks precision. Channels will be fabricated in silicon to achieve straight side walls, which are able to sustain acoustic standing waves better than curved surfaces of isotropically etched glass.

In summary, LSBAW microchannels offer promising capabilities for particle and cell enrichment and separation at the microscale; however, further investigation, both in simulation and in experiments, is needed to reach the full potential of this technology.

References

1. B. D. Plouffe, S. K. Murthy, L. H. Lewi, Fundamentals and application of magnetic particles in cell isolation and enrichment: a review, *Rep. Prog. Phys.* 2015, 78(1), 016601

2. M. Toner, D. Irimia, *Blood-on-a-chip, Annu. Rev. Biomed. Eng.* 2005, 7, 77-103

3. J. Takagi, M. Yamada, M. Yasuda, M. Seki, Continuous particle separation in a microchannel having asymmetrically arranged multiple branches, *Lab. Chip.* 2005, 5, 778-784

4. M. Yamada, K. Kano, Y. Tsuda, J. Kobayashi, M. Yamato, M. Seki, T. Okano, "Microfluidic devices for size-dependent separation of liver cells, *Biomed. Microdevices.* 2007, 9, 637-645

5. M. D. Vahey, J. Voldman, An equilibrium method for continuous-flow cell sorting using dielectrophoresis, *Anal. Chem.* 2008, 80, 3135-3143

6. I. Cheng, V. E. Froude, Y. Zhu, H. Chang, H, Chang, A continuous high-throughput bioparticle sorter based on 3D traveling-wave dielectrophoresis, *Lab. Chip.* 2009, 9, 3193-3371

7. J. Voldman, M. Toner, M. L, Gray, M. A. Schmidt, Design and analysis of extruded quadrupolar dielectrophoretic traps, *J. Electrost*, 2003, 57, 69-90

8. B. M. Taff, J. Voldman, A scalable addressable positive-dielectrophoretic cell-sorting array, *Anal. Chem.* 2005, 77, 7976-7983

9. R. Huang, T. A. Barber, M. A. Schmidt, R. G. Tompkins, M. Toner, D. W. Bianchi, R. Kapur, W. L. Flejter, A microfluidics approach for the isolation of nucleated red blood cells (NRBCs) from the peripheral blood of pregnant women, *Prenat. Diagn.* 2008, 28, 892-899

10. M. A. M. Gijs, Magnetic bead handling on-chip: new opportunities for analytical applications, *Microfluid. Nanofluid.* 2004, 1, 22-40

11. A. Winkleman, K. L. Gudiksen, D. Ryan, G. M. Whitesides, D. Greenfield, M. Prentiss, A magnetic trap for living cells suspended in a paramagnetic buffer, *Appl. Phys. Lett.* 2004, 85, 2411-2413

12. Q. Ramadan, V. Samper, D. Poenar, C. Yu, Magnetic-based microfluidic platform for biomolecular separation, *Biomed. Microdevices.* 2006, 8, 151-158

13. A. H. B. de Vries, B. E. Krenn, R. van Driel, J. S. Kanger, Micro magnetic tweezers for nanomanipulation inside live cells, *Biophys. J.* 2005, 88, 2137-2144

14. M. P. MacDonald, G. C. Spalding, K. Dholakia, Microfluidic sorting in an optical lattice, *Nature.* 2003, 426, 421-424

15. G. Milne, D. Rhodes, M. MacDonald, K. Dholakia, Fractionation of polydisperse colloid with acousto-optically generated potential energy landscapes, *Opt. Lett.* 2007, 32, 1144-1116

16. C. Piggee, Optical tweezers: not just for physicists anymore, *Anal. Chem.* 2009, 81, 16-19

17. A. N. Grigorenko, N. W. Roberts, M. R. Dickinson, Y. Zhang, Nanometric optical tweezers based on nanostructured substrates, *Nature. Nanotechnology.* 2008, 2, 365-370

18. D. G. Grier, A revolution in optical manipulation, *Nature.* 2003, 424, 810-816

19. M. Evander, L. Johansson, T. Lilliehorn, J. Piskur, M. Lindvall, S. Johansson, M. Almqvist, T. Laurell, J. Nilsson, Noninvasive acoustic cell trapping in a microfluidic perfusion system for online bioassays, *Anal. Chem.* 2007, 79, 2984-2991

20. M. Wiklund, S. Nilsson, H. M. Hertz, Ultrasonic trapping in capillaries for trace-amount biomedical analysis, *J. Appl. Phys.* 2001, 90, 421-426

21. M. Wiklund, H. M. Hertz, Ultrasonic enhancement of bead-based bioaffinity assays, *Lab. Chip.* 2006, 6, 1279-1292

22. M. Wiklund, C. Gunther, R. Lemor, M. Jager, G. Fuhr, H. M. Hertz, Ultrasonic standing wave manipulation technology integrated into a dielectrophoretic chip, *Lab. Chip.* 2006, 6, 1537-1544

23. X. Ding, S.-C. S. Lin, B. Kiraly, H. Yue, S. Li, I. K. Chiang, J. Shi, S. J. Benkovic, T. J. Huang, On-chip manipulation of single microparticles, cells, and organisms using surface acoustic waves, *Proc. Natl. Acad. Sci. U. S. A.* 2012, 109, 11105-11109

24. J. Shi, D. Ahmed, X. Mao, S.-C. S. Lin, A. Lawit, T. J. Huang, Acoustic tweezers: patterning cells and microparticles using standing surface acoustic waves (SSAW), *Lab. Chip.* 2009, 9, 2861-3024

25. C. W. Shields IV, C. D. Reyes, G. P. Lopez, Microfluidic cell sorting: a review of the advances in the separation of cells from debulking to rare cell isolation, *Lab. Chip.* 2015, 15, 1230-1249

26. H. Bruus, Acoustofluidics 7: The acoustic radiation force on small particles, *Lab. Chip.* 2012, 12, 1014-1021

27. W. T. Coakley, D. W. Bardsle, M. A. Grundy, F. Zamani, D. J. Clarke, Cell manipulation in ultrasonic standing wave fields, *J. Chem. Technol. Biotechnol.* 1989, 44, 43-62

28. H. M. Hertz, Standing- wave acoustic trap for nonintrusive positioning of microparticles, *J. Appl. Phys.* 1995, 78, 4845-4849

29. F. Petersson, A. Nilsson, C. Holm, H. Jonsson, T. Laurell, Separation of lipids from blood utilizing ultrasonic standing waves in microfluidic channels, *Analyst.* 2004, 129, 938-943

30. F. Petersson, A. Nilsson, C. Holm, H. Jonsson, T. Laurell, Continuous separation of lipid particles from erythrocytes by means of laminar flow and acoustic standing wave forces, *Lab. Chip.* 2005, 5, 20-22

31. F. Petersson, L. Aberg, A. M. Sward-Nilsson, T. Laurell, Free flow acoustophoresis: microfluidic-based mode of particle and cell separation, *Anal. Chem.* 2007, 79, 5117-5123

32. H. Bruus, Acoustofluidics 1: Governing equations in microfluidics, *Lab. Chip.* 2011, 11, 3742-3751

33. P. Tabeling, *Introduction to Microfluidics*, Oxford University Press, Oxford, 2005

34. H. Bruus, *Theoretical Microfluidics*, Oxford University Press, Oxford, 2008

35. F. M. White, *Viscous Fluid Flow*, McGraw Hill Education Press, 2011

36. D. T. Blackstock, *Fundamentals of Physical Acoustics*, John Wiley & Sons, Inc. 2000

37. L. E. Kinsler, A. R. Frey, A. B. Coppens, J. V. Sanders, *Fundamentals of Acoustics*, John Wiley & Sons, Inc. 2000

38. L. V. King, On the acoustic radiation pressure on spheres, *Proc. R. Soc.* 1934, 147, 212-240

39. K. Yosioka, Y. Kawasima, Acoustic radiation pressure on a compressible sphere, *Acustica*, 1955, 5, 167-173

40. L. P. Gor'kov, On the forces acting on a small particle in an acoustical field in an ideal fluid, *Sov. Phys. Dokl.* 1962, 6, 773-775

41. M. A. H. Weiser, R. E. Apfel, E. A. Neppiras, Interparticle forces on red-cells in a standing wave field, *Acustica*, 1984, 56, 114-119

42. L. K. Zarembo, *High-intensity ultrasonic fields* (Plenum Press, New York, USA, 1971), chap. Acoustic Streaming, ed.: L. D. Rosenberg

43. H. Schlichting, *Boundary-layer theory*, Springer-Verlag Berlin Heidelberg, 2017

44. L. Rayleigh, On the circulation of air observed in Kundt's tubes, and on some allied acoustical problems, *Phil. Trans. R. Soc. London*, 1883, 175, 1-21

45. C. Eckart, Vortices and streams caused by sound waves, *Phys. Rev.* 1948, 73, 68-76

46. J. T. Karlsen, H. Bruus, Acoustic tweezing and patterning of concentration fields in microfluidics, *Phy. Rev. Applied.* 2017, 7, 034017

47. M. Evander, A. Lenshof, T. Laurell, J. Nilsson, Acoustophoresis in wet-etched glass chips, *Anal. Chem.* 2008, 80, 5178-5185

48. J. Dual, D. Moller, Piezoelectricity and application in the excitation of acoustic fields for ultrasonic particle manipulation, *Lab. Chip.* 2012, 12, 506-514

49. R. Barnkob, P. Augustsson, T. Laurell, H. Bruus, Measuring the local pressure amplitude in microchannel acoustophoresis, *Lab. Chip.* 2010, 10, 563-570

50. L.S.L Cheung, X. Zheng, A. Stopa, J. C. Baygents, R. Guzman, J. A. Schroeder, R. L. Heimark, and Y. Zohar, Detachment of captured cancer cells under flow acceleration in a bio-functionalized microchannel. *Lab. Chip*, 2009, 9(12), 1721-1731.

51. L. M. Lee, R. L. Heimark, J. C. Baygents, and Y. Zohar, 2006. Self-aligned immobilization of proteins utilizing PEG patterns. *Nanotechnology*, 2006, 17(4), S29.

52. P. Glynne-Jones, R. J. Boltryk, M. Hill, Modelling and applications of planar resonant devices for acoustic particle manipulation, *Lab. Chip.* 2012, 12, 1417-1426

53. E. J. Fong, A. C. Johnston, T. Notton, S. Y. Jung, K. A. Rose, L. S. Weinberger, M. Shusteff, Acoustic focusing with engineered node locations for high-performance microfluidic particle separation. *Analyst*, 2014, *139*(5), 1192-1200.

54. I. Leibacher, P. Hahn and J. Dual, 2015. Acoustophoretic cell and particle trapping on microfluidic sharp edges. *Microfluidics and Nanofluidics*, 2015, *19*(4), 923-933.